Renewable Energy 182 (2022) 1060–1079

Contents lists available at ScienceDirect

Renewable Energy

journal homepage: www.elsevier.com/locate/renene

Exploring inflow wind condition on floating offshore wind turbine aerodynamic characterisation and platform motion prediction using blade resolved CFD simulation

Yang Zhou [a], Qing Xiao [a, *], Yuanchuan Liu [b], Atilla Incecik [a], Christophe Peyrard [c], Decheng Wan [d], Guang Pan [e], Sunwei Li [f]

[a] Department of Naval Architecture, Ocean and Marine Engineering, University of Strathclyde, Glasgow, G4 0LZ, UK
[b] College of Engineering, Ocean University of China, Qingdao, 266100, PR China
[c] Saint-Venant Hydraulics Laboratory (Électricité de France, ENPC, Cerema), Université Paris-Est, 6 quai Watier, 78400, Chatou, France
[d] Computational Marine Hydrodynamic Lab, State Key Laboratory of Ocean Engineering, School of Naval Architecture, Ocean and Civil Engineering, Shanghai Jiao Tong University, Shanghai, 200240, China
[e] School of Marine Science and Technology, Northwestern Polytechnical University, Xi'an, 710072, PR China
[f] Division of Ocean Science and Technology, Graduate School at Shenzhen, Tsinghua University, Shenzhen, 518055, Guangdong, PR China

ARTICLE INFO

Article history:
Received 11 January 2021
Received in revised form
27 July 2021
Accepted 2 November 2021
Available online 10 November 2021

Keywords:
Turbulent wind
Computational fluid dynamics (CFD)
Floating offshore wind turbine (FOWT)

ABSTRACT

The present study is aimed at investigating the effect of turbulent wind and shear wind on the floating offshore wind turbine (FOWT) structure by using a high-fidelity computational fluid dynamics (CFD) method. This method is believed to resolve the wind field around the turbine blades, wake and the near air-wave free-surface regime, allowing us to have a more in-depth examination into both aerodynamic and hydrodynamic of the FOWT. In the present study, the modelling of a coupled aero-hydro-mooring FOWT system is focused on a temporal and spatial variable turbulent wind field by using a time-varying spectrum, which has not been examined for a floating wind turbine. The turbulent wind in the study is generated with Mann's wind turbulence model, while the Von Karman wind spectrum is used to represent wind turbulence. In addition, different wind shears were also examined. We can conclude from this study that, when turbulent wind is present, there are fluctuations in both the rotor thrust and power outputs associated with the non-uniform wake region although the time-mean magnitude is almost the same. In addition, turbulence wind lead to a quicker wake diffusion than time-independent inflow wind. Furthermore, the existence of wind shear results in an even larger decrease in the local minimum thrust/power about 2–6% when the turbine blade is passing in front of the tower. Despite this, under the present wind inflow conditions, the inline surge force, dynamic motion, and the mooring tension of the floater are not significantly affected by either the turbulence wind or the wind shear.

1. Introduction

In recent years, the concept of FOWT has been rapidly developing as it is claimed that these FOWT systems can offer a better solution to wind energy compared to their counterpart onshore wind turbines, for example, Hywind-Scotland [1], the first commercial offshore wind farms achieves 65% of capacity factor, which is much higher than a typical bottom-fixed offshore or onshore wind turbine with a capacity of 30%–45%. Numerical analysis is one of many key tools during the initial FOWT design stage. Through the application of numerical analysis, we are able to predict the aero/hydrodynamic performance of a coupled FOWT system. Nonetheless, the main challenge is being able to replicate these results under real environmental wave and wind conditions.

Some of the most commonly used methods accustomed to analyse the aerodynamic of a wind turbine include: low-cost Blade Element Method (BEM) and high-fidelity, high-cost Computational Fluid Dynamics (CFD). Due to the fact that CFD allows us to directly solve the fluid flow governing equations, we are able to use it to produce detailed flow variables in both the time and spatial

* Corresponding author.
E-mail address: qing.xiao@strath.ac.uk (Q. Xiao).

https://doi.org/10.1016/j.renene.2021.11.010

domains so that the transient aerodynamic loading on the tower, turbine blade, and the wind wake structure can all be well resolved. For a typical FOWT, the operating wind speed and the size of the FOWT contribute to changing the airflow into turbulent regime. This means that CFD modelling for a FOWT must factor in the turbulent feature. There are three general approaches for turbulence modelling. These are: Large Eddy Simulation (LES), Direct Numerical Simulation (DNS) and Unsteady Reynolds-Average Navier-Stokes (URANS). Recently, a hybrid model named Improved Delayed Detached Eddy Simulation (IDDES) is developed [2], in which URANS is employed in the near wall treatment and LES model is used in the far field. Due to the fact that IDDES predicts more accurate solutions on wind turbine aerodynamics while owes a lower computational cost than the LES, it has been applied in several research areas including wind turbine. However, a quick review on the IDDES [3–5] papers for wind turbine investigation indicated that all studies are focused on either a bottom-fixed wind turbine or a floating system with prescribed pitch and surge motions. Therefore, the *free-motion* of floating structure is entirely excluded in their studies. This is also an indicator that the applicability and reliability of IDDES on the numerical prediction of ocean waves and the wave-structure interaction problems have not been fully validated and verified. Therefore, out of these approaches, URANS is considered as the most efficient method due to its relatively low computational cost while also having reasonably good predictions for the time-mean variables.

As of right now, most FOWT turbulent CFD analysis simplifies the problem by assuming a uniform and constant incoming wind field. However, in a non-controlled environment, the real wind field is much more unpredictable and considered as a stochastic process, which varies in both temporal and spatial domains. To allow us to replicate conditions of wind turbulence such that they reflect a real life scenario, spectral methods are commonly used so that we can reproduce such a turbulent wind field. Here, the given wind spectrum is broken down into a set of turbulent components with various wave numbers and frequencies. One of the commonly used approaches is addressed by Veers [6] based on the observation of Atmospheric Boundary Layer (ABL) spectra to provide three-dimensional turbulent components over homogeneous terrain. This method has been adopted in the National Renewable Energy Laboratory (NREL) TurbSim code [7]. It has also been coupled alongside NREL FAST [8] to model the aero-hydro-servo-mooring FOWT system under turbulent inflow conditions. Another technique used is the Mann wind turbulence model [9] which utilizes a velocity spectral tensor to predict a second-order three-dimensional fully turbulent field. Mann's method is able to accurately and efficiently simulate the homogeneous inflow and ABL turbulence [10,11].

Previous studies into the understanding of the impact that turbulence has on a wind turbine began onshore before progressing onto offshore fixed and floating systems. Li et al. [12] utilized the Mann wind turbulence model to analyse a bottom-fixed wind turbine aided by CFD code (CFDship-Iowa). The study found that the wake diffusion would increase in the presence of turbulence. By using a simple actuator line theory and LES modelling, Troldborg et al. [13] investigated the effect of both uniform and turbulent wind conditions on a bottom-fixed wind turbine. This was also done using the Mann wind turbulence model and a simplified wind turbine model. His study revealed that when wind turbulence is present, the wake is found to be more unstable than if turbulence was absent. As we get closer to the turbine rotor, we can see this effect become increasingly more prominent in this region. In addition to this, the study found that the disparity under various wind turbine-modelling methods is negligible. Knowing that the wind turbulence will have a significant impact on the wind farm performance, Olivares et al. [14] analysed the modelling of homogeneous turbulence inflow in the turbine wake through utilizing actuator disk (AD) theory and LES modelling. His study showed that the velocity field within the wake region becomes uniform whilst the turbulence kinetic energy increases behind the AD model. This effect can be attributed to the existence of the AD edges. In addition to this, Chivaee et al. [15] performed a study in which he investigated a 2D air-foil under turbulent wind by using the LES method and the Sub-Grid Scale (SGS) model. His research extended to the fixed wind turbine wake under turbulent wind. We can see from his work that the blade tip vortices could be captured accurately under fine mesh resolution. Contrary to this, the coarse mesh provides rather poor wake predictions. Moreover, Grinderslev et al. [16] compared the onshore wind turbine aerodynamic performance considering the turbine flexibility under turbulent inflows using LES and IDDES models, his study revealed that there is no significant difference between both methods on the prediction of separate flows and blades deflection.

Moving from onshore to offshore floating wind turbine concepts, recent research conducted by Li et al. [17] focuses on a semi-submersible NREL 5 MW FOWT using the BEM tool under different wind inflow conditions. His results show that the existence of a turbulent wind field led to a very unstable thrust force and power. By using a high-fidelity LES method to solve the wind turbine aerodynamic and a low-fidelity potential theory based method to predict the floating platform hydrodynamic, Doubrawa et al. [18] conducted an investigation on the hydrodynamic loads of a Hywind Spar floating wind turbine under turbulent wind conditions with the use of Simulator for Offshore Wind Farm Applications (SOWFA) and NREL FAST. Their results demonstrated that with the aid of the stochastic wind turbulence models, the fatigue loads were overestimated at low wind speeds (0–8 m/s) but underestimated at high wind speeds (over 25 m/s).

Other than the turbulence wind nature mentioned above, in a wind farm area in real life, wind field shear layer is regarded as another key factor which will have an impact on the wind turbine aerodynamic. The onshore wind turbine can be seen to be greatly influenced by this factor due to the boundary layer development on land. Dolan and Lehn [19] performed a wind shear study on an onshore wind turbine with a comprehensive model based on analytical formulations. They concluded that wind shear resulted in a slight reduction of the power of the rotor compared to uniform wind. This reduction then became more significant when exposed to tower shadow effects [20]. These effects could also be seen in the work conducted by Wen et al. [21] through using the Free Vortex Method (FVM). Gould et al. [22] discovered the pitch moment difference of the onshore wind turbine subjected to a series of shear winds based on a momentum-based method. Their research revealed that when the wind shear layer thickness was gradually increased, a higher shear-induced pitch moment could be seen and caused further fatigue damages to the wind turbine. Recent research by Li et al. [17] using BEM to examine the wind shear on FOWT concluded that, although wind shear has a minor influence on the total power outputs of the rotor, the local aerodynamic loads fluctuations caused by wind shear produced additional fatigue damage loads onto the root of blade.

Admitting that the impact of the inflow wind turbulence or wind shear on the aerodynamic performance of the wind turbine have been examined in aforementioned studies, however, most of them are conducted either on a bottom-fixed offshore wind turbine or an onshore wind turbine. For a floating wind turbine, the effects of the inflow wind conditions may play an important role and reveal new characteristics near the wave-air surface, and also the *floating* moored structure caused by the aero-hydro-mooring coupling. These features are entirely excluded for a fixed wind turbine or for a prescribed platform motions as studies in Refs. [23,24].

Although some of the recent research has considered the FOWT subjected to turbulent wind conditions, those research regarding the effects of turbulent inflow and shear wind on the wind turbine used simplified methods to model the effect on the blades, such as BEM or AL/AD models. In addition, some researchers applying a prescribed surge/pitch motion onto a FOWT tower to represent the motion of a floater. In addition, as FOWT is a complex system, it is hard to study such fully coupled aero-hydro-mooring problem using any laboratory testing to combine all factors into consideration. i.e., turbulent wind aerodynamics, ocean wave hydrodynamics, floating structure motion response, and mooring system. Therefore, at current stage, the numerical modelling plays a significant role on FOWT investigations for identifying the main parameter matrix and guiding the design of laboratory testing.

The current study investigates the behaviour of a FOWT under the influence of a turbulent wind field generated by the incoming wind spectrum in addition to the shear wind field. As mentioned earlier, the blade-resolved flow examination in addition to the motion capturing of free floater, allow us to understand both the aerodynamic and hydrodynamic details of FOWT. However, these have not been accounted for in previous studies conducted. The current perception is that turbulent wind may have an effect on both the unsteady aerodynamic loading of the wind turbine and the hydrodynamic response of the floater. The existence of wind shear may cause variance in the local aerodynamic characteristics and the pitch moment of the FOWT. These effects may result in an overall performance change of the turbine. The aim is achieved by using our in-house hydro-aero-mooring CFD tool [25–28], which is able to fully resolve the flow flied details around the turbine blades and the area where wave-air has strong interaction with the free surface. The Mann wind turbulence model is also adopted to replicate the turbulent wind. The magnitude and spatial distribution of the turbulence are put in as boundary condition inputs to the CFD solver. The modelling of a FOWT under regular wave conditions is then carried out in our numerical wave tank. After this, the aero/hydrodynamic responses are computed before being compared to the values predicted by the BEM tool.

2. Numerical methodology

2.1. Flow solver

2.1.1. Governing equations of fluid flow

The open source Computational Fluid Dynamics framework OpenFOAM [29] is applied as the flow solver for the duration of the coupled FOWT simulation. The governing continuity and momentum equations for a transient, incompressible flow can be written as,

$$\nabla.\mathbf{U}=0 \tag{1}$$

$$\frac{\partial\rho\mathbf{U}}{\partial t}+\nabla.\left(\rho\left(\mathbf{U}-\mathbf{U_g}\right)\mathbf{U}\right)=-\nabla P_t-\mathbf{g}.\mathbf{x}\nabla\rho+\nabla\left(\mu_{eff}\nabla\mathbf{U}\right)+(\nabla\mathbf{U}).\nabla\mu_{eff}+\mathbf{f_\sigma} \tag{2}$$

where $\mathbf{U}$ and $\mathbf{U_g}$ represent the velocity of the flow field and grid nodes in Cartesian coordinates, respectively; ρ refers to the mixed density of water and air, g denotes the gravity acceleration; $P_t=P-\rho\mathbf{g}.\mathbf{x}$ is the dynamic pressure obtained by the total pressure P minus the hydrostatic pressure $\rho\mathbf{g}.\mathbf{x}$; We can use the formula $\mu_{eff}=\rho\ (\nu+\nu_t)$ to calculate the effective dynamic viscosity, in which ν and ν_t are the kinematic and eddy viscosity respectively; $\mathbf{f_\sigma}$ represents the surface tension.

2.1.2. Turbulence modelling

The k-ωSST (Shear Stress Transport) turbulent model is used to account for a high Reynolds number. This may reach values as high as Re $=10^7$ for a typical wind turbine. As indicated by previous studies, the k-ωSST turbulence model [30] is made up from a combination of the standard k-ωmodel and the k-εmodel. To be specific, it combines the standard k-ωmodel found near the structure boundary layer and changing to the k-εmodel in the far-field. This design shows its strengths in adverse pressure gradients and predicting separating flow.

For the governing equations for turbulent kinetic energy (TKE) k and the specific dissipation rate ω, we can show that,

$$\frac{\partial\rho k}{\alpha t}+\nabla.(\rho\mathbf{U}k)+\nabla.(\Gamma_k\nabla\mathrm{k})+\tilde{P_k}-D_k=0 \tag{3}$$

$$\frac{\partial\rho\omega}{\alpha t}+\nabla.(\rho\mathbf{U}\omega)+\nabla.(\Gamma_\omega\nabla\omega)+P_\omega-D_\omega+Y_\omega=0 \tag{4}$$

where Γ_k and Γ_ω denotes the effective diffusivity of the turbulent kinetic energy k and the specific dissipation rate ω respectively; $\tilde{P_k}$ and P_ω refers to the turbulence production terms, and D_k and D_ω are the turbulence dissipation terms;Y_ω is the cross-diffusion term introduced by blending the standard k-$\omega$and k-εmodels.

2.1.3. Free surface modelling

To allow capturing of the air-water free surface, the Volume of Fluid (VOF) method [31] is applied in OpenFOAM, in which the free surface is represented by the volume fraction α . For a two-phase air-water fluid flow, the volume fraction is distributed as follows,

$$\begin{cases}\alpha=0,\ air\\ \alpha=1, water\\ 0<\alpha<1, free\ surface\end{cases} \tag{5}$$

The governing equations of the volume fraction variable αfollows,

$$\frac{\partial\alpha}{\alpha t}+\nabla.\mathbf{u}\alpha+\nabla.[\mathbf{u_r}(1-\alpha)\alpha]=0 \tag{6}$$

In order to capture the free surface accurately, a bounded compression method with an additional compression term on the left-hand side of the transport equations has to be introduced which only functions near free surface due to the inclusion of $(1-\alpha)\alpha$, where $\mathbf{u_r}=\mathbf{u_{water}}-\mathbf{u_{air}}$ is an artificial velocity field, and used to compress the interface.

For a multiphase flow problem, the volume fraction of each liquid is used as the weighting factor to calculate the mixture properties. Listed below are the equations for the density and the viscosity,

$$\rho=\alpha\rho_l+(1-\alpha)\rho_g \tag{7}$$

$$\mu=\alpha\mu_l+(1-\alpha)\mu_g \tag{8}$$

where the subscripts l and g refer to the liquid and gas respectively.

2.1.4. Wave generation and absorbing

To generate regular waves in our numerical wave tank, an open-source toolbox "waves2Foam" [32] has to be used. A new boundary condition at the inlet boundary was implemented in the Open-FOAM to generate different types of numerical waves based on the relevant wave theories. In addition, the relaxation zone was adopted to provide better wave quality whilst also avoiding wave reflection in the absorbing zones. This technique is applied at both the inlet and outlet boundaries in the numerical wave tank. The main functions of the relaxation zones are specified as follows,

$$\alpha_R(\chi_R) = 1 - \frac{\exp(\chi_R{}^{3.5}) - 1}{\exp(1) - 1} \tag{9}$$

$$\varphi_R = \omega_R \varphi_R^{computed} + (1 - \omega_R)\varphi_R^{target} \tag{10}$$

where φ_R represents either the velocity or volume fraction of water α; the definition of χ_R is that the weighting functions α_R is always equal to 1 at the interface between the non-relaxed computational domain and the relaxation zones, while χ_R refers to a value between 0 and 1.

In the present work, the stokes second order regular wave theory is adopted in the present study which is widely used in ocean waves modelling. The surface elevation can be represented into the time domain by the following equation,

$$\eta(x,t) = A\cos\delta + \frac{A}{16}\frac{Agk}{\omega}\frac{\cosh kh}{\sinh^3 kh}cosh(2kg+2)\cos 2\delta \tag{11}$$

where A represents the wave amplitude; ω is the angular frequency; φ denotes the wave phases; h refers to the water depth and k is the wave number.

The vertical and horizontal velocities w and u implemented to the inlet boundary are given by,

$$w(x,t) = \frac{Agk}{\omega}\frac{\sinh k(z+h)}{\cosh(kh)}sin\delta + \frac{3}{4}\frac{Agk}{\omega}\frac{AH}{2\lambda}\frac{\sinh 2k(z+h)}{\cosh^4(kh)}\sin 2\delta \tag{12}$$

$$u(x,t) = \frac{Agk}{\omega}\frac{\cosh k(z+h)}{\cosh(kh)}cos\delta + \frac{3}{4}\frac{Agk}{\omega}\frac{AH}{2\lambda}\frac{\cosh 2k(z+h)}{\cosh^4(kh)}\cos 2\delta \tag{13}$$

g is the gravitational acceleration; z refers to the vertical length measured upwards from the still water level; h is the water depth and λ representing the wavelength.

2.1.5. Mooring line modelling

A mooring system analysis module is implemented into the coupled aero-hydro-mooring system under the CFD framework [26], where both the quasi-static [33] and the dynamic mooring line modules are developed. The dynamic method is then adopted in order to capture more accurate results, as we take into account any dynamic effects which include inertial forces compared with quasi-static mooring line modelling.

Typically, the mooring lines are not directly simulated in the CFD computational domain. Instead, the tension loads of the mooring lines are added as constraints on the patches of the floater onto the computational mesh. In order to capture the tension loads subjected to the mooring lines, a 3D-lumped mass method is adopted to perform the dynamic mooring line behaviour. The sketch of the dynamic mooring line modelling is shown in Fig. 1.

In a 3D-lumped mass model, the mooring lines are discretized into n+1 nodes (concentrated masses) which are connected by n springs (massless segments). All the nodes have to satisfy the equilibrium equations and elongation equations both in the horizontal and vertical directions. At the beginning of the simulations, the initial tension forces at the first segment connected with the platform are specified as the estimated total weight of the mooring lines in water. In addition, the positions of mooring anchor are always checked at each unsteady time step to guarantee the predicted mooring anchor position is consistent with the constraints imposed by the anchor. If the convergence criterion is satisfied of the error functions, then the tension loads of each segment is determined.

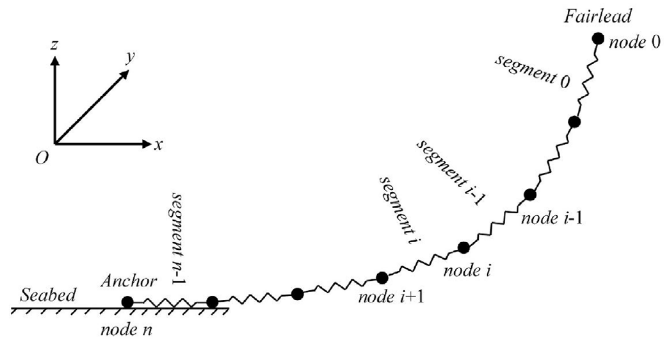

Fig. 1. 3D Lumped-mass dynamic mooring line modelling.

In order to calculate the hydrodynamic loads on the mooring lines exerted by the fluid flow (which is neglected during the CFD modelling), Morison's equations [34] are adopted in the mooring system analysis module. Both the drag force and virtual mass force (inertial force) is computed. This is done firstly for line segments and then transformed to the adjacent nodes.

2.2. Turbulent wind modelling

To solve the problem of turbulent wind modelling, the Mann [9] method is implemented into the current flow solver. As we can see in Mann's method, the Mann wind turbulence box is based off the construction of a velocity-spectrum tensor (φ_{ij}) of a neutral atmospheric boundary layer (ABL). The turbulence field is then reproduced with second-order statistics derived from two things, either from the covariance tensor or from its Fourier transform. Generally, they are relevant to the spectral tensor (i.e. Von Karman tensor in the present study). However, the stochastic velocity field $u(x)$ does not have a direct Fourier transform as it is unable to be integrated over the space. Mann's velocity field can be represented in terms of a generalized Fourier-Stieltjes integral

$$\mathrm{u}(\mathrm{x}) = \int e^{i\kappa.x} d\mathbf{Z}(\kappa) \tag{14}$$

In which κ represents the wave number vector and the integration of κ covers all the wave number space which makes up the velocity field; $\mathbf{Z}(\kappa)$refers to a complex orthogonal stochastic process. We can then use this process to calculate the velocity-spectrum tensor φ_{ij}

$$\varphi(x)_{ij} d\kappa_1 d\kappa_2 d\kappa_3 = d\mathbf{Z}_i^*(\kappa) d\mathbf{Z}_j(\kappa) \tag{15}$$

where * stands for the conjugate and *represents averaging. Because the velocity-spectrum tensor φ_{ij} is related to its covariance three-dimensional energy spectrum, if the flow is thought to be incompressible, the spectral tensor can then be given by the formula,

$$\varphi_{ij}(\kappa) = \frac{E(\kappa)}{4\pi\kappa^4}\left(\delta_{ij}\kappa^2 - \kappa_i\kappa_j\right) \tag{16}$$

The Von Karman spectrum [35] is selected for use in the current study as it is one of the recommended energy spectrums in the International Electrotechnical Commission (IEC). This is given as,

$$E(\kappa) = \alpha\varepsilon^{2/3}L^{5/3}\frac{L^4\kappa^4}{\left(1 + L^2\kappa^2\right)^{17/6}} \tag{17}$$

where α is the Kolmogorov constant,ε is the rate of dissipation of turbulent kinetic energy (TKE) and L represents a length scale. As it is currently impossible to measure the energy spectrum experimentally, we must utilize one-dimensional spectra which can be derived after following the relationship with three-dimensional spectrum [36]. The one-dimensional Von Karman spectrum can be expressed as follows, for the spectrum relating to longitudinal direction,

$$F_1(\kappa_1) = \frac{9}{55}\alpha\varepsilon^{2/3}L^{5/3}\frac{1}{\left(1 + L^2\kappa_1^2\right)^{5/6}} \tag{18}$$

For the spectrum of transversal direction (i = 2,3),

$$F_i(\kappa_1) = \frac{3}{110}\alpha\varepsilon^{2/3}L^{5/3}\frac{3 + 8L^2\kappa_1^2}{\left(1 + L^2\kappa_1^2\right)^{11/6}}(i = 2, 3) \tag{19}$$

2.3. Implementation wind turbulence to flow solver

$$x = L_1 - U_{mean}t \tag{20}$$

The Mann wind turbulence method described above has been built into our coupled hydro-aero-mooring CFD solver. We can see how it is implemented into the simulation in Fig. 2. There are three

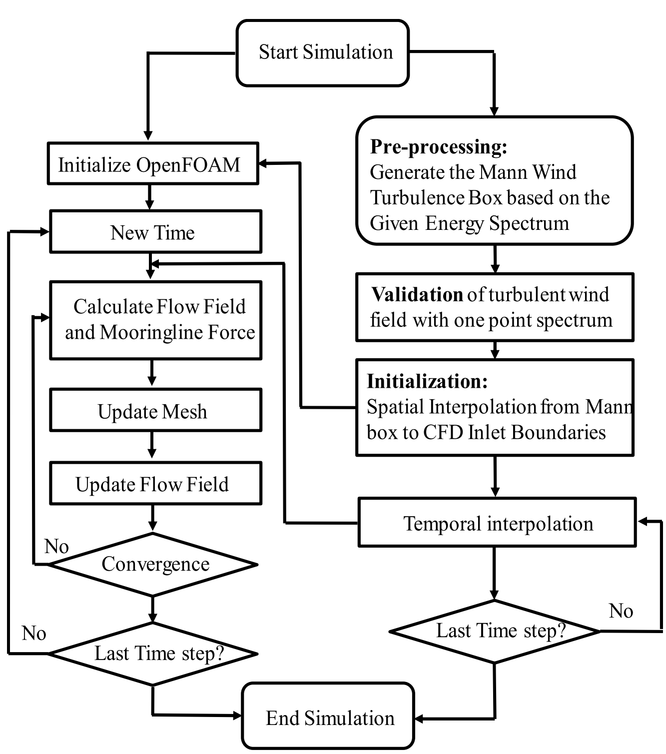

Fig. 2. Layout of the implementation of Mann model to OpenFOAM.

main steps to this. Firstly, the homogeneous isotropic turbulence wind field has to be generated. Fast Fourier transform is utilized to compute the velocity field with the given one-dimensional spectra, i.e., equations (18) and (19). After doing so, we are able to generate a three-dimensional field with this data. Taylor's frozen hypothesis is used to transfer time series into space series. Based on this, velocities are extracted from different sections of the Mann wind turbulence box, and various time-domain results can be obtained along a transversal plane in the Mann box. The relationship between a longitudinal dimension and time is given as.where L_1 is the longitudinal dimension of the Mann wind turbulence box and U_{mean} stands for the mean wind velocity at a specific turbine hub height. The generated turbulence wind field has to be evaluated against the given wind power spectrum first before they are inserted as the wind turbulent boundary conditions onto the CFD computational domain. Because the CFD mesh is finer than the discretized wind field in Mann wind turbulence box, a trilinear interpolation is required. This allows us to obtain all relevant turbulent velocities at the CFD mesh along the inlet boundary. Another key factor is that as the unsteady CFD modelling time step is significantly shorter compared to the time step used for the turbulent wind field generation, a similar time interpolation is also required.

3. Validation and verification

3.1. The implementation of Mann wind turbulence model

The study conducted below validates the generation of the turbulence wind field based on Mann's algorithm. Firstly, the results are compared against the one-point velocity spectra, previously defined in Equations (18) and (19). The mean velocity is established as the rated wind speed at 11.4 m/s of an NREL 5 MW wind turbine. The Mann wind turbulence box domain is defined as $Lx \times Ly \times Lz = 2400m \times 500m \times 300m$. The length increment of the domain cells is set to $10m$ in both the longitudinal and transversal directions. The velocity distribution at the turbine hub (i.e., Y = 0 m and Z = 90 m) along the three directions are displayed in Fig. 3 along with the spectra produced as a result of the Mann model. The velocities vary throughout the entirety of the spatial domain, i.e. $Um\pm3m/s$, $Vm\pm2m/s$, $Wm\pm1.5m/s$ for the longitudinal and transversal velocity respectively. Fig. 3 shows the comparison between the theoretical transversal velocity one-point velocity spectra against the spectrum obtained from the Mann model. The values Su, Sv, and Sw represent the spectrum calculated on the u, v, and w velocities respectively. Fig. 4 presents the velocities at various axial positions in the CFD domain without the FOWT structure where the decay of turbulence could be seen due to the nature of URANS numerical method.

Fig. 5 shows the standard deviation of the velocity distribution along the XoY and XoZ planes perpendicular to the Z-axis and Y-axis while the turbine rotor locates at Z = 90 m and Y = 0 m. As we can see from Fig. 5, the standard deviation calculated from the Mann model remains consistent with the given one point spectrum. The standard deviation in x, y and z velocity is fluctuated near 1.0 m/s, 0.7 m/s, 0.5 m/s, respectively. These values satisfy the IEC standard [37] of $\sigma_2 \geq 0.7\sigma_1$, $\sigma_3 \geq 0.5\sigma_1$. Despite this, the turbulence intensity (TI) follows IEC standard of TI = 0.12 for axial velocity.

3.2. Dynamic motion response and aerodynamic performance of FOWT

The present hydro-aero-mooring CFD solver has been validated through several OC4 Semi-submersible NREL-5 MW FOWT studies

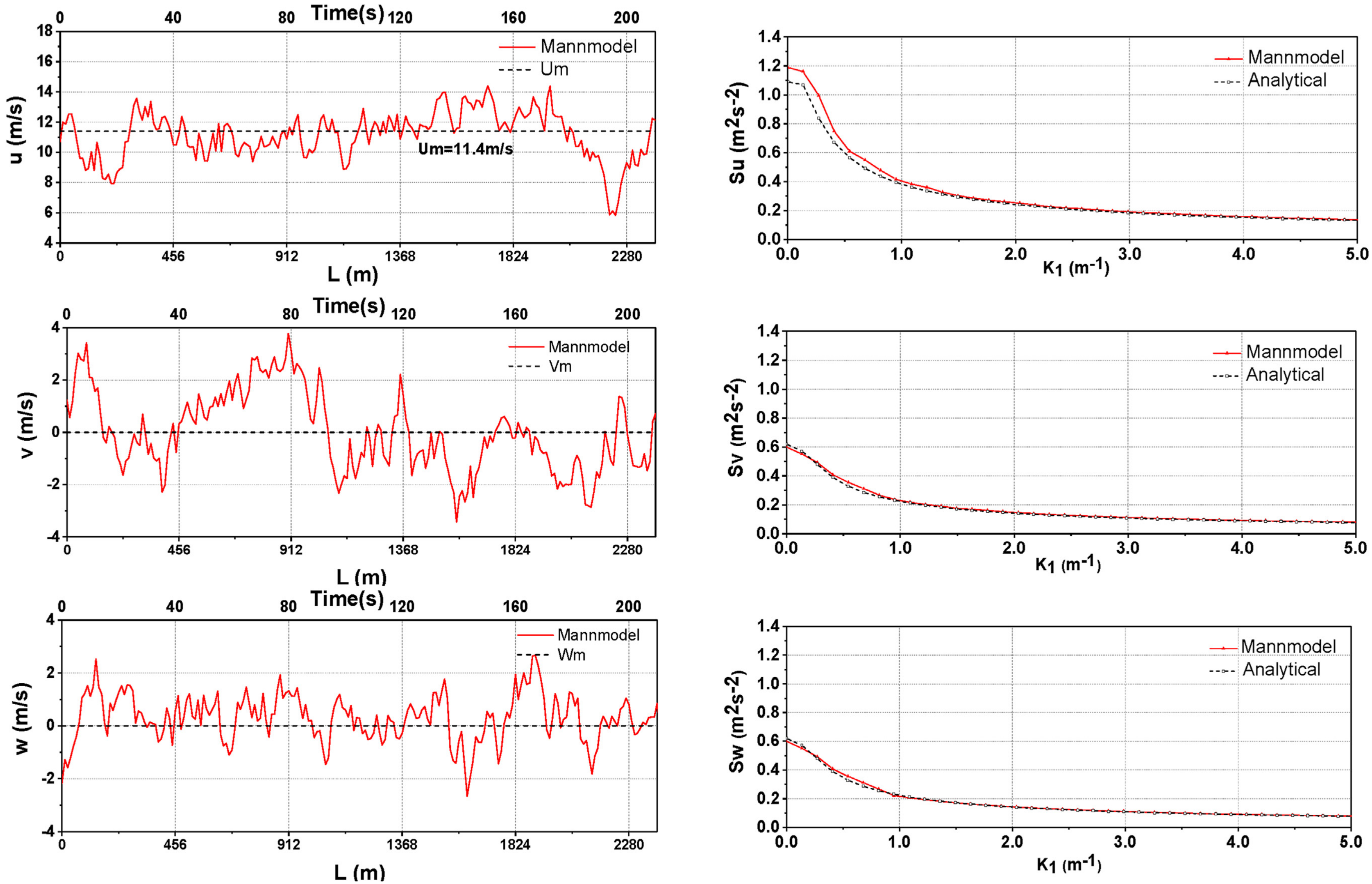

Fig. 3. Mann model validation left: velocity distribution along three directions at hub location; right: one-dimensional velocity spectra for each velocity component computed from Mann model.

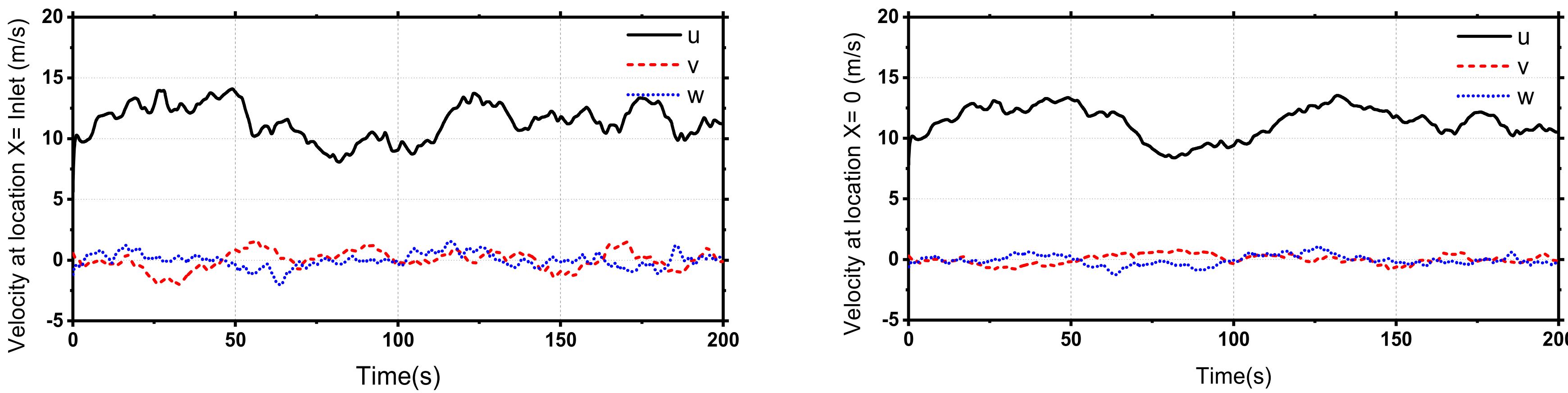

Fig. 4. Time history of velocities at turbine hub height (Z = 90 m) in inlet boundary (X = −250 m in Fig. 10) and rotor plane positions (X = 0 m) in CFD calculation without FOWT structure.

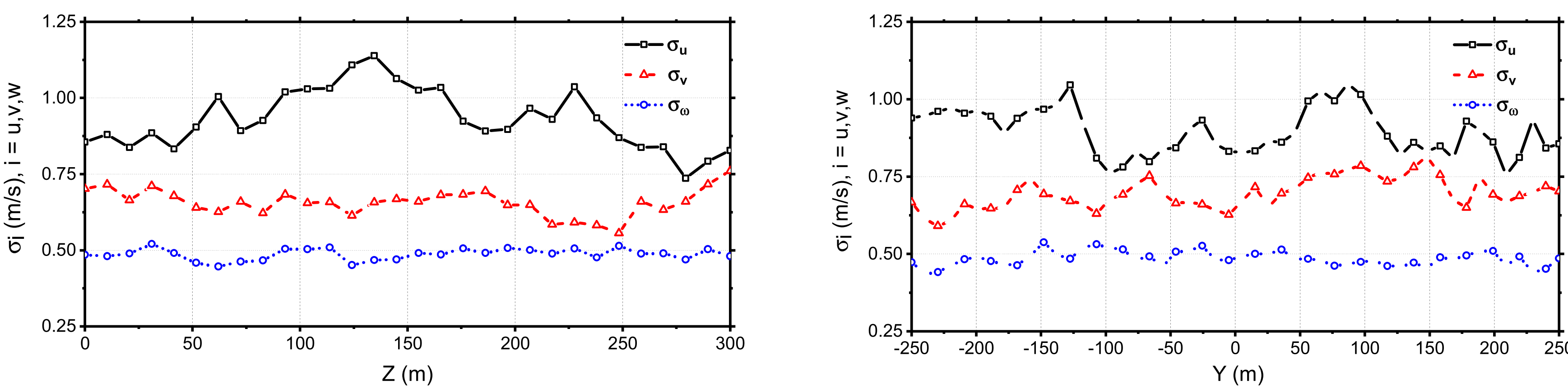

Fig. 5. Standard deviation of flow field along the XoY & XoZ plane perpendicular.

which can be seen in our previous papers [25–27]. These validations against an 1/50 scaled model operated cover the hydrodynamic responses of the floating structures, the aerodynamic performance of the wind turbine and the tension loads of the mooring lines under both regular wave with a uniform wind field.

In the present study, we carried out a validation study with the operating conditions provided in Ref [38]. The uniform inflow speed is 7.32 m/s while the rotor speed is fixed as 4.95 RPM with a collective blade pitch angle of 6.4°. The NREL 5 MW wind turbine aerodynamics are investigated without considering the floating platform and the supporting tower.

Fig. 6 summarizes the time history aerodynamic thrust in 30 s. Three meshes with different densities are generated, which are termed as Coarse (3.8 million), Medium (5.7 million) and

Fine (10.3 million). The time-averaged value is calculated from 20 s to 30 s to eliminate the initial start-up effects. It can be clearly seen that the difference for thrust between different mesh is nearly negligible, indicating that the results are independent of the grid. Moreover, the current predictions are in a good agreement with the experimental data as shown in Table 1.

As the turbulent wind field has been previously validated in section 3.1, thus, we carried out one more mesh sensitivity study regarding the coupled aero-hydro-mooring FOWT system considering the floating substructures and the tower under uniform inflow and regular wind conditions, i.e., LC1.1 (see Table 2 for the operation conditions parameters). This mesh number refers to 2.7 million, 6.8 million, and 8.6 million for coarse, medium, and fine respectively. Fig. 7 summarizes the time history of the rotor thrust and power predictions under one sampled rotation period, the aligned results indicate that the results are mesh independent. Thus, taking the computational cost into consideration, the medium size of the mesh utilized for the following simulations. To model the present turbulent wind rather

4. Numerical setup

4.1. Case setup

The model used in this study is the OC4 semi-submersible NREL 5 MW floating offshore wind turbine. In regards to the bottom component, the DeepCwind semi-submersible platform is made up of three offset columns with large heave plate bases, with one centre column used to support the wind turbine and several connecting braces which act together to stabilize the floater. The wind turbine subsections include the rotor blades, hub, nacelle, and the

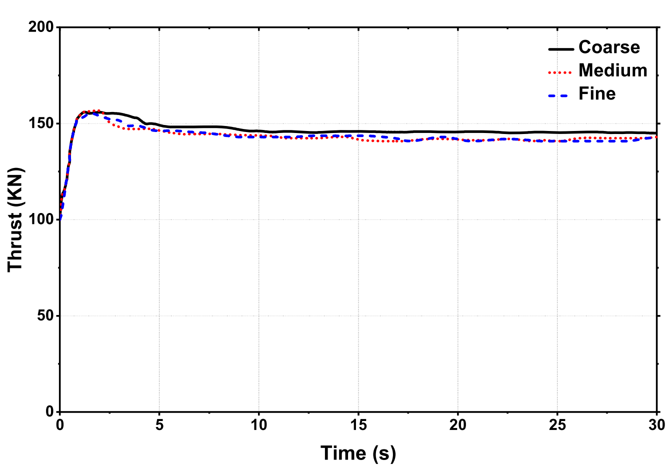

Fig. 6. Time history of NREL 5 MW wind turbine thrust force.

Table 1
Mesh sensitivity results of aerodynamic thrust of NREL 5 MW wind turbine.

Mesh	Number	CFD	Experimental	FAST
Coarse	3.8 million	143.8 KN	126.1 KN	102.6 KN
Medium	5.7 million	142.0 KN		
Fine	10.3 million	140.8 KN		

tower. The rotor diameter is 126.0 m and the hub height is 90 m above the still water line (SWL).

4.2. Selected case studies

In the present study, four different wind fields are examined while the wave condition is kept constant throughout. A schematic diagram showing these four wind fields is plotted in Fig. 8 and listed in Table 2. Three time-independent wind inflow conditions are examined, one uniform inflow (LC1.1) and two shear wind inflows (LC2.1 and LC2.2). The turbulent wind, illustrated in Fig. 8 is time-dependent as LC3.1. For the time-independent shear wind, the shear layer is picked up as 25 m in LC2.1, and 90 m in LC2.2. The 25 m height is a height which can be found in other investigations [14], however, 90 m is selected for two reasons. Firstly, in the LC2.1, H = 25 m is too short to fully cover the region where the turbine blades rotate, thus, we anticipate that the influence of such shear flow on the aerodynamic characteristics of the wind turbine is minimal. The LC2.2 with H = 90 m is expected to yield significantly different results from LC2.1. In addition, to study the turbulence incoming wind, the Mann turbulence box generates a shear layer between H = 0 (SWL) to the turbine rotor centre at H = 90 m. Therefore, LC2.2 is set up in this study. The time-mean velocity U_m is 11.4 m/s. The wave condition for all four cases is Stokes second-order regular wave as wave height and wave period refers to 7.58 m and 12.1 s, the commonly used sea state in North Sea [38]. The blade pitch angle is maintained as a constant of 0° and the rotor speed is fixed to 12.1 RPM under rated wind speed suggested by NREL [39]. The turbine blades are regarded as rigid, and thus no aero-elasticity of blade is taken into account and also no blade pitch and generator torque controller are used in the present model.

4.3. Computational domain and boundary conditions

As was previously mentioned, the dimensions of the CFD domain are different from those of the Mann turbulence box as we can see in Table 3. As shown, the X and Y dimensions of the Mann turbulence box are larger than those of the CFD as suggested in Refs. [12,15,40]. This allows us to achieve the spatial interpolation of the turbulent velocity field originally generated in the Mann box. However, the Z dimension of the Mann turbulence box is smaller than that of CFD domain. This is due to the inclusion of the water wave phase in CFD modelling, e.g. a water depth of 200 m is included.

A built-in arbitrary mesh interface (AMI) method in OpenFOAM can be used to analyse the motion of an OC4 semi-submersible NREL 5 MW FOWT. Fig. 9 shows the partial mesh on the structure and AMI surface of the entire computational domain. A built-in tool (snappyHexMesh) has been adopted to generate the computational mesh. The total mesh for the present CFD computation for all four simulations equates to 6844520. Grid refinement is applied near the free surface where the wind turbine blades and the turbine wake can be found. Eight layers of boundary layer mesh with the first layer grid thickness of 0.4 mm and a progression rate of 1.1 is added. This is to ensure the y + value is in the range of [30,300] while a wall function is adopted for near wall treatments. In

Table 2
Physical properties of the selected cases.

Wind Fields	Uniform	Shear 1	Shear 2	Turbulence
Load Cases	LC1.1	LC2.1	LC2.2	LC3.1
Waves	Regular wave: **H=7.58m, T=12.1s**			
Wind: Wind fields				
Characteristics	Time-independent	Time-dependent		
Equations	$U_0(x,y,z,t) = \overline{U_m}\left(\frac{z}{H}\right)^n$			
$\overline{U_m}$ (m/s)	$\overline{U_m} = 11.4$	$\overline{U_m} = \overline{U_m}(x,y,z,t) = 11.4$		
H (m)	90	25	90	90
n	0	1	1	1

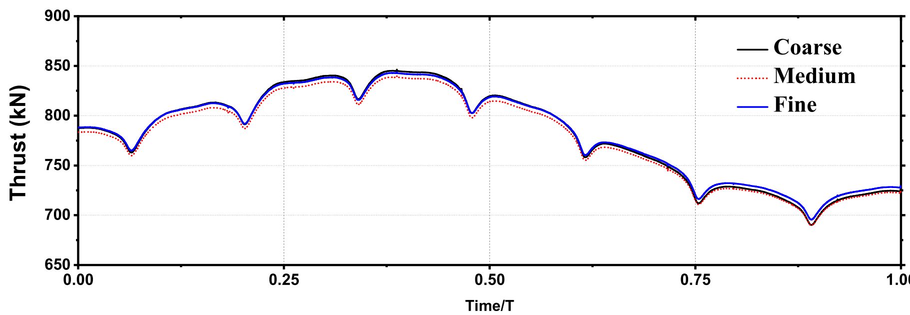

Fig. 7. Time history of NREL 5 MW wind turbine thrust under regular waves. than constant wind, additional mesh refinement is conducted, and the detail is introduced in section 4.2.

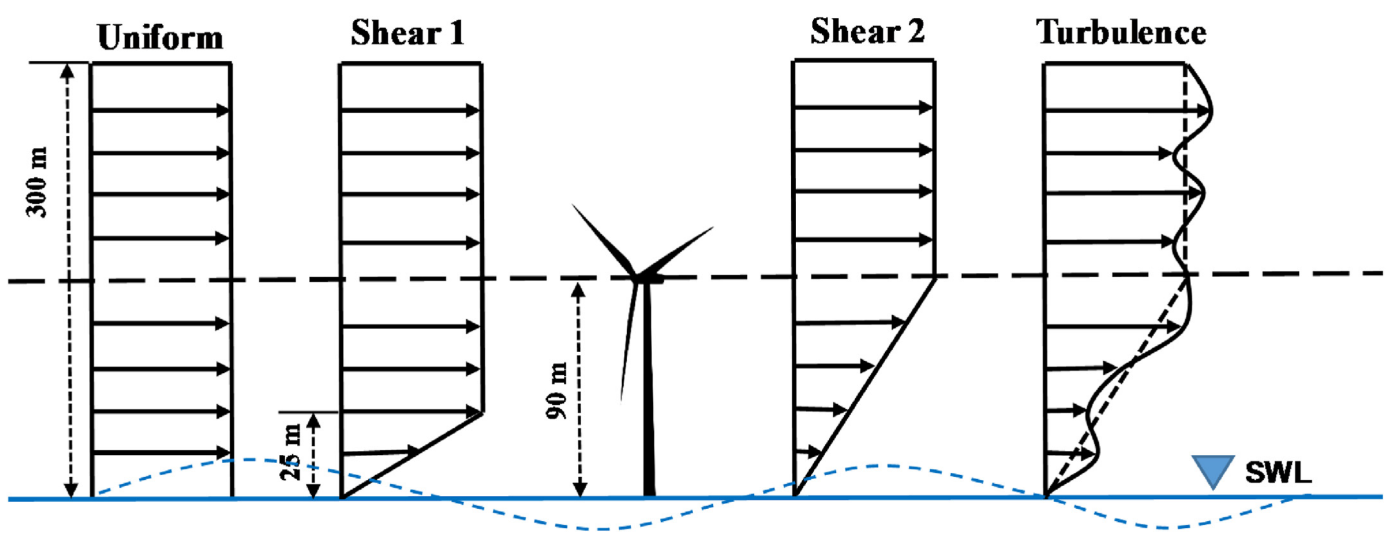

Fig. 8. Sketch of four wind fields.

Table 3
Main parameters of the CFD computational domain and Mann turbulence box, d refers to the spacing of offset columns of platform (50 m).

	OpenFOAM (CFD)	Mann Turbulence Box
Domain Size	$750m \times 400m \times 500m$	$15D \times 8D \times 10D$
	$2400m \times 500m \times 300m$	$48D \times 10D \times 6D$
Domain Grid	6844520 *cells*	$240 \times 50 \times 30$ *cells*
Grids around WT	3549010 *cells*	N/A

addition, relaxation zones are set to achieve a better wave quality and to reduce the wave reflection. The length of these zones are defined as follows, i.e., inlet relaxation zones: one wave length, and the outlet relaxation zones: two wave lengths. The origin of the coordinate system is located at the FOWT platform centre and the flow direction is along the positive x-axis.

The sketch of the boundary conditions of CFD domain is shown in Fig. 10. At the inlet boundary (where $x = -250m$), the velocity is defined as the prescribed incident regular wave together with up turbulent, uniform and shear winds. The κ and ω, is estimated by using Equations (18) and (19) referred by Tian's study [41], where I is the turbulence intensity and $\frac{\mu_t}{\mu}$ represents the viscosity ratio.

$$\kappa = 1.5(UI)^2 \tag{18a}$$

$$\omega = \frac{\rho\kappa}{\mu}\frac{\mu_t}{\mu}^{-1} \quad (19a$$

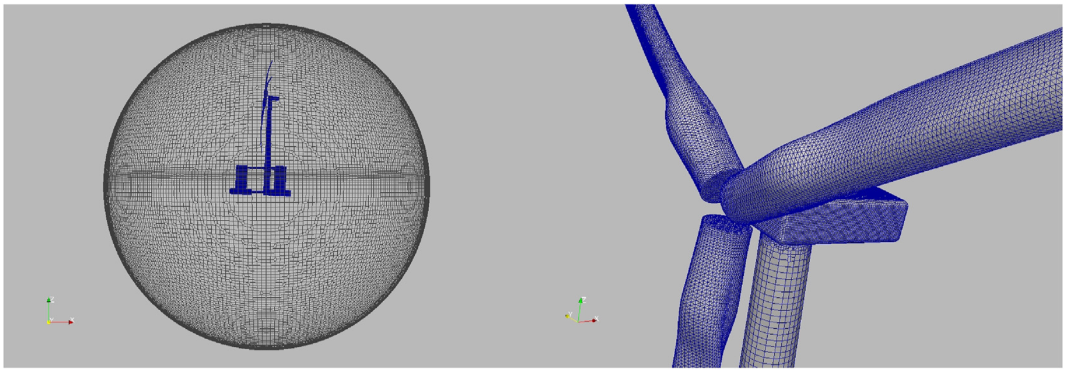

Fig. 9. Computational mesh of NREL 5 MW semi-submersible FOWT.

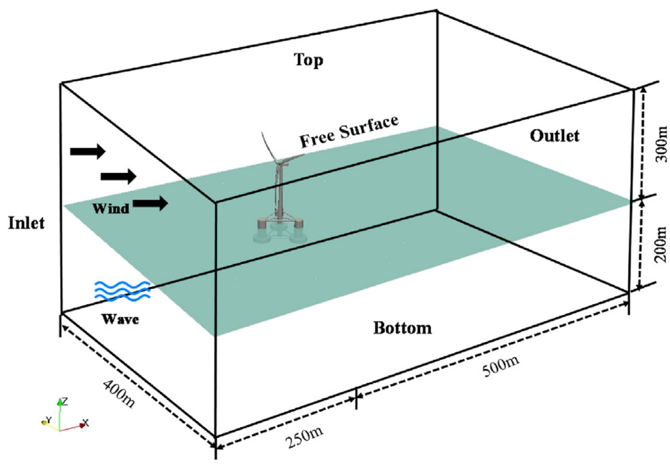

Fig. 10. Sketch of CFD computational domain of FOWT modelling.

The gradient of velocity, κ and ω is set to zero at the outlet boundary ($x = 500m$). The front and back boundaries ($y = \pm 200m$) are imposed symmetrically and the top and bottom boundaries ($z = 300m$ and $-200m$) are set as the zero gradient. The non-slip wall boundary with zero pressure gradient is defined on the patches of the FOWT.

The time step is set as small as 0.001s, i.e., 1/4950 of T_{rot} for one turbine rotation, 1/12100 of one wave period. For LC1.1, LC2.1, LC2.2 and LC3.1, it takes nearly 580 h using High Performance Computing facility with 200 cores running in parallel for 200 s, i.e., the time span covers around 40 rotations for a wind turbine or 17 incident wave periods.

5. Results

5.1. Wind turbine aerodynamics

Fig. 11 shows the time history of the rotor thrust and power predictions under two sampled wave periods (132s–156s) when they are exposed to uniform, shear and turbulent flow conditions. Then, by utilizing both NREL FAST V8 and TurbSimV1.06 [8,42], we are able to compare these results against the BEM results achieved previously. We know that the instantaneous time is non-dimensionalized by the incident wave period (T), whilst an estimate of the thrust force of CFD can be calculated by using the sum of the aerodynamic force exerted on all three blades along the x direction. Consequently, the power can also be calculated by multiplying the rotor torque against the angular velocity of the rotor blades. Non-dimensionally, the formula: $C_T = Thrust/0.5\rho RU^2$ can be used to work out the thrust coefficient. Similarly, the power coefficient can be estimated by applying the formula $C_p = Power/0.5\rho RU^3$, in which, R represents the rotor radius and U stands for the wind speed.

Referring to Fig. 11 again, we can see that the values for both CFD and NREL FAST display a similar pattern in regards to the rotor thrust force and the overall power output of the wind turbine. Under uniform inflow conditions (LC1.1), the thrust and power outputs show a similar pattern, i.e., the numerical predicted peak values are smaller than those obtained from FAST. This might be due to the fact that the floater motion on the turbine wake flow is taken into consideration via solving the URANS equations directly, while the BEM based tool (NRAL FAST) adopts an empirical correction dynamic wake model. Similar findings are noted in References [12,43,44] where the variance of the peak thrust/torque is nearly ±8%. In the present simulation, the difference goes to nearly 11%. At certain time instances, (0.06 T, 0.20 T, 0.33 T, 0.47 T, etc.), we are able to see a few local minimum values appear along both thrust force and power curve simultaneously. From the data, we can see that these sudden dips vary between 5 and 7% of the mean thrust force and power. These can be observed at every 1/3 rotation of the wind turbine, where the blades rotation aligns themselves front of the tower.

The results obtained by comparing different wind fields suggests that in the presence of wind turbulence, both the peak of the thrust and power is increased when compared against a time-independent uniform/shear wind. In addition to this, CFD is able to predict a larger magnitude of fluctuation than the FAST results. Aside from this, however, it is also observed that there is a relatively low frequency variation in the thrust and power, which could potentially be directly caused by the turbulent decay which is associated with the URANS CFD modelling used in this study.

To allow us to develop a better understanding of the consequence that turbulent wind has on the aerodynamic performance of a wind turbine, we must carry out a statistical analysis of the data. The results of this analysis can be seen, summarized above in Table 4 for the peak and time-mean parameters. We can see that the Time-mean thrust results obtained by using CFD indicate that despite the mean magnitude being nearly identical for the uniform, shear wind and turbulent wind, (e.g. 783.7 KN, 781.3 KN, 771.73 KN, 781.3 KN for LC1.2, 2.1, 2.2 and 3.1 respectively), the standard deviation values for turbulent wind (LC3.1) is seen to be reasonably larger than the values obtained for the time-independent wind field, i.e., 39.7 KN, 40.5 KN and 43.8 KN for LC.1.1, 2.1 and 2.2, respectively. This observation can also be found in the results of the NREL FAST analysis. On top of this, the difference between the peak thrust and power between uniform and turbulent wind is also

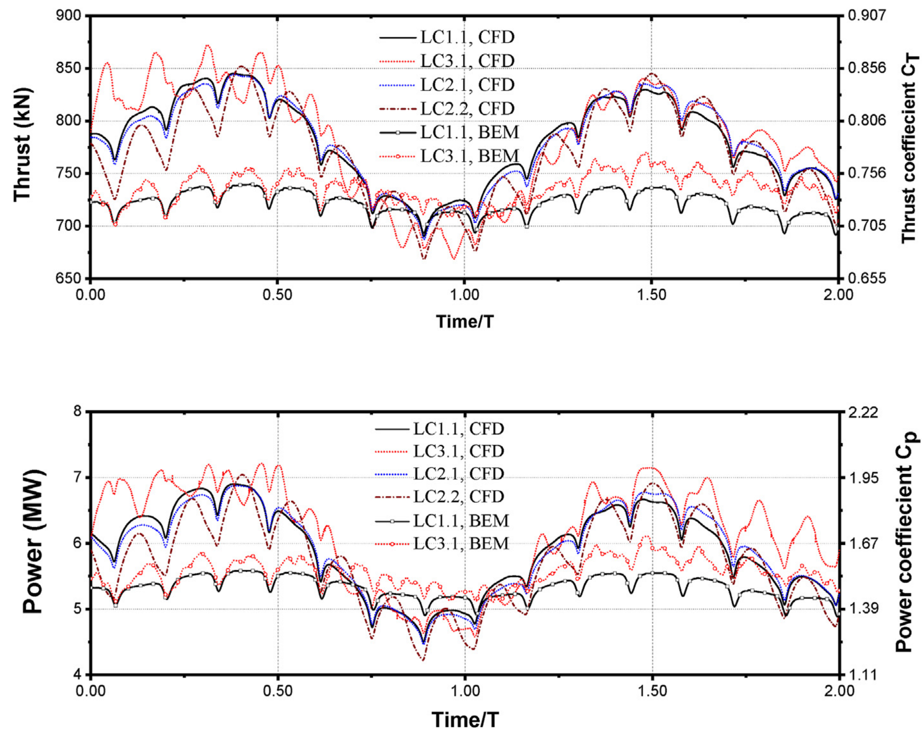

Fig. 11. Thrust and power outputs of FOWT under uniform, shear and turbulent flow.

Table 4
Statistics of thrust and power of wind turbine under different wind fields.

CFD						NREL FAST	
		Uniform wind (LC1.1)	Shear wind (LC2.2)	Shear wind (LC2.1)	Turbulent wind (LC3.1)	Uniform wind (LC1.1)	Turbulent wind (LC3.1)
Thrust (KN)	Max/Diff	846.4 (0.00%)	845.1 (− 0.15%)	851.8 (0.65%)	872.2 (3.05%)	739.8 (0.00%)	770.4 (4.13%)
	Min/Diff	690.3 (0.00%)	687.4 (− 0.43%)	668.3 (− 3.19%)	668.6 (− 3.14%)	693.2 (0.00%)	701.1 (1.14%)
	Mean/Diff	781.3 (0.00%)	781.3 (0.00%)	771.7 (− 1.22%)	783.7 (0.31%)	723.2 (0.00%)	735.1 (1.65%)
	σ	39.7	40.5	43.8	53.1	10.2	14.3
Power(MW)	Max/Diff	6.90 (0.00%)	6.87 (− 0.43%)	7.04 (2.02%)	7.21 (4.49%)	5.58 (0.00%)	6.11 (9.49%)
	Min/Diff	4.50 (0.00%)	4.46 (− 0.80%)	4.22 (− 6.02%)	4.58 (1.70%)	4.90 (0.00%)	5.10 (4.08%)
	Mean/Diff	5.88 (0.00%)	5.89 (0.17%)	5.75 (− 2.21%)	6.16 (4.76%)	5.34 (0.00%)	5.54 (3.74%)
	σ	0.63	0.64	0.67	0.76	0.15	0.21

slightly larger than their respective time-mean values. However, it should be taken into account that the thrust and power are both largely controlled by the wind speed that locates at the upstream region of the rotor blades. Because of this, the large time-variable peak thrust which was found in the presence of turbulence does not necessarily suggest that the time-mean thrust is larger in the absence of turbulence.

5.2. Wind turbine wake profile

Fig. 12 below shows the instantaneous velocity contour on a horizontal XoY plane at Z = 90 m where we can see the effects of either the presence or absence of turbulence at a time instant *t=0.9T*. The initial FOWT positions are coloured in black which proves that the floating structures are interacted with the turbine wake. At these specific values, we can see exactly where the rotor thrust output reach a trough in Fig. 11. The vorticity plots rendered as the ISO surfaces of Q is set to 1. This is coloured by the axial velocity [45]. Using the data and comparing all four figures, a typical spatial variation can be clearly seen and alongside this, there are some clear-cut differences between uniform/shear wind conditions and turbulent wind conditions. In the presence of turbulence, we can see that, the wind field upstream of the wind turbine clearly shows a lower speed regime time sequence is plotted, at the point where t = 0.9 T, the instantaneous thrust value when turbulence is present is less than the instantaneous thrust value calculated when turbulence is absent. This smaller value in the instantaneous thrust can be attributed to the low speed regime upstream of the wind turbine. This effect can also explain why the wake downstream of the turbine looks to be more unsteady and non-uniform. As a result of this, the turbulent diffusive nature is observed to extend further down into to the weaker vortices forming between the hub and the blades.

Fig. 13 shows the vertical sectional view with respect to the flow field at the mid-plane (XoZ) of the computational domain. We can see that both in the absence and presence of turbulence, at two specific time instances, (i.e., t = 0.9 T and t = 1.4 T) the minimum and maximum thrust is generated, while also factoring in the free surface of water-air. From Fig. 13, we can see the airflow close to the air-wave free surface is significantly more affected by the water wave propagation compared to the airflow which is further away. This represents the wind-wave interaction which is coupled in the CFD modelling. This observable effect can be attributed to the decreased air velocity which can be seen above both the wave

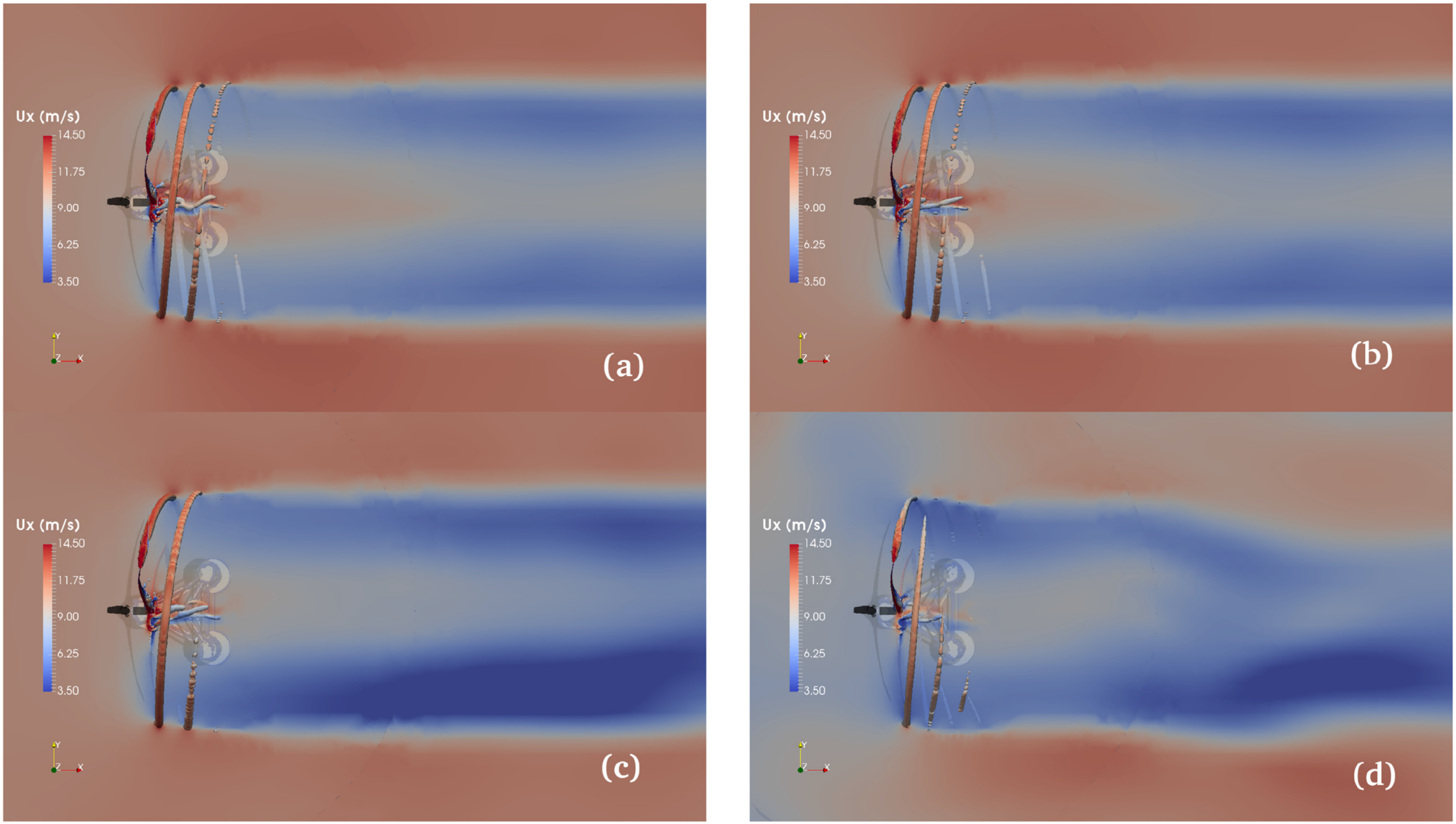

Fig. 12. Instantaneous flow field in a horizontal sectional plane coloured by axial velocity located at the hub height (z = 90 m) at instant time of 0.9 T. (a): LC1.1, (b): LC2.1, (c): LC2.2, (d): LC3.1.

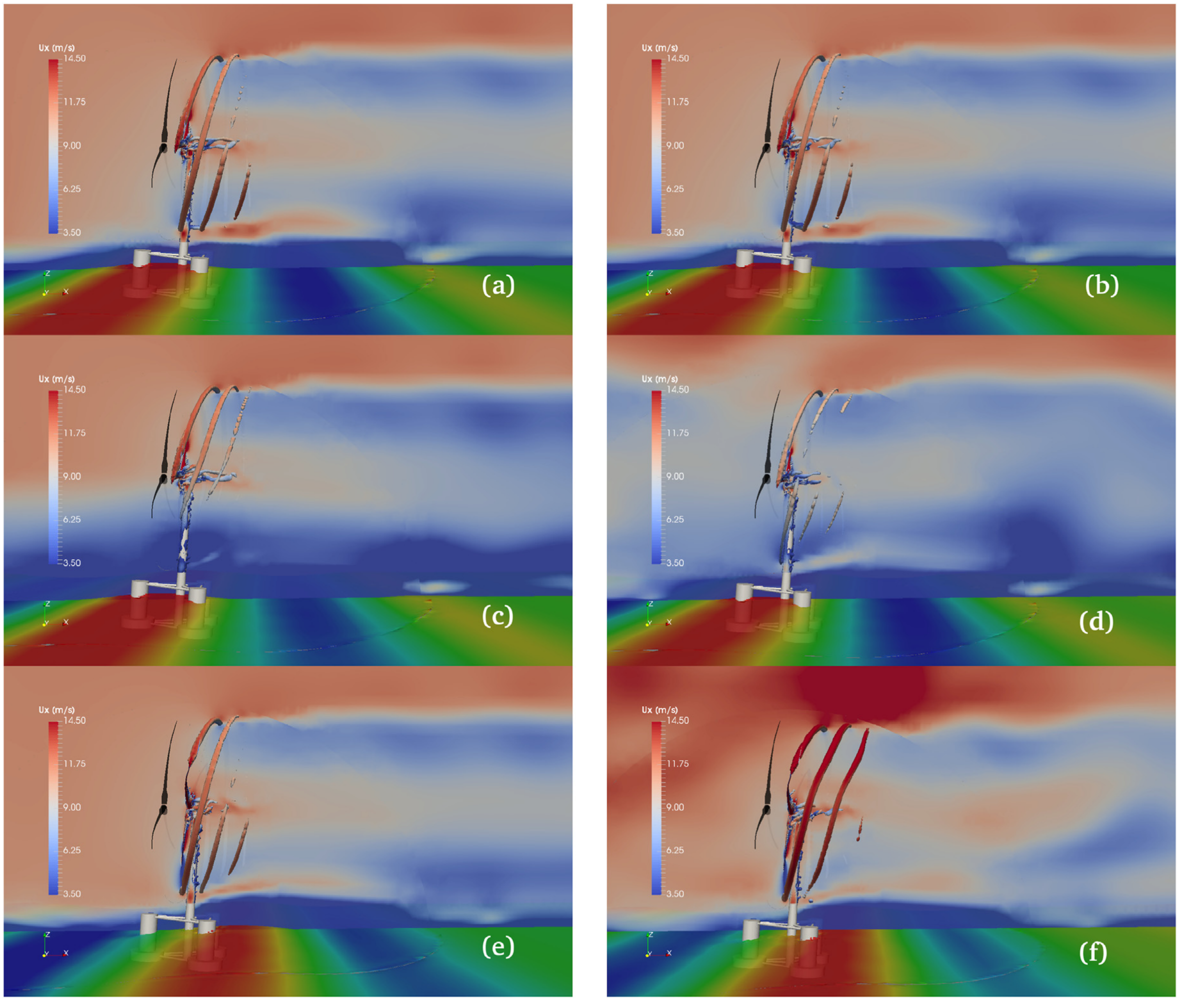

Fig 13. Instantaneous flow field in a sectional vertical mid-plane (XoZ) coloured by axial velocity: (a) LC1.1 (b) LC2.1 (c) LC2.2 (d) LC3.1 at time t=0.9T; (e) LC1.1 (f) LC3.1 at time t=1.4T

crests and troughs near the free surface. It should not go unmentioned the airflow field found around the wind turbine is not significantly affected. Similar to the findings from Fig. 12, we can see that the turbine wake at the *XoZ* plane (which is represented by the velocity field) becomes increasingly non-uniform when turbulence is present compared to the conditions when turbulence is absent. Fig. 14 shows the axial velocity distribution when a non-dimensionless form is present U/U_∞ in the wake region ranging from $x = 0.5D_{rtr}$ to $3.0D_{rtr}$ downstream. Using Fig. 14, we are able to see the velocity found at the rotor, (i.e., $y/D_{rtr} = 0$), decreases apparently from the near-wake to the far wake, whilst the velocity found at both the top and bottom blade tips, i.e., $y = \pm 0.5D_{rtr}$ are found to trend closer to the rated wind speed. In addition, we can see that when compared against the time-independent wind fields (LC1.1, LC2.1 and LC2.2), the presence of wind turbulence (LC3.1) results in quick diffusion of the wake. This is demonstrated by a rapid change of axial velocities between $-0.5D_{rtr} < Y < 0.5D_{rtr}$. These findings are supportive to the studies by Li et al. [12] for an onshore fixed wind turbine, e.g. the floating concepts have negligible impacts on the turbine wake velocity distribution along the horizontal sectional plane at hub height when they are compared with onshore turbines.

Fig. 15 plots the instantaneous turbulence intensity (TI) contour at the $Y = 0$ m plane. Since the results gathered from LC1.1, LC2.1 and LC2.2 are almost identical to each other, the only comparison that can be made is between conditions with uniform wind (LC1.1) and conditions with turbulent wind. We can see that the plots above in Fig. 15 show a large variation in the TI regime. This variation is not unique to only the rotor as it can also be found at the tip of the blade. More detailed information regarding the variation can be seen in Fig. 16, where the turbulence intensity profiles are recorded at the hub height. We can see here that, similar to the velocity profile shown in Fig. 14, the TI also dissipates faster for LC3.1. It should be noted however, that at the blade tip of $y = \pm 0.5D_{rtr}$, the TI value is found to be greater in the presence of turbulence than in the absence of turbulence.

Fig. 17 shows the contours of the airflow field at four different span-wise sections of blade-1, i.e., the blade of the turbine with an azimuth angle of 0°. This is coloured by the axial velocity. Fig. 18 shows the pressure distribution along the surface of foils, represented by Cp alongside the schematic diagram which indicates the slices along the blade span direction. This is represented by *r/R*. Factoring in the aspect that no aero-elastic feature of the blade is taken into account for the conducted simulation, the Angle of Attack (AoA) of the varying slices of the blade is constant. These values are provided in the NREL report [39]. As shown in Fig. 17 (a), the flow separation occurs between 1/3 to 1/2 chord lengths from the foil leading edge under all conditions and at varying *r/R* levels.

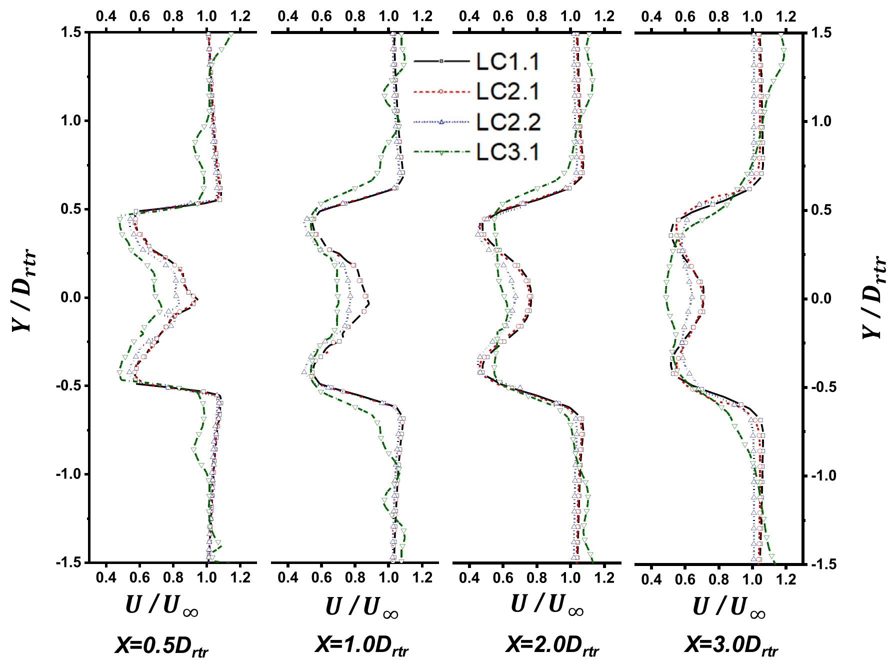

Fig. 14. Axial velocity at different axial positions at hub height (Z = 90 m) in the wake region at t = 0.9 T.

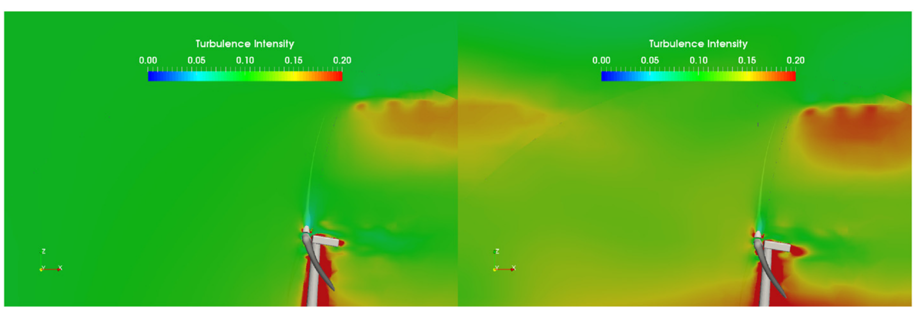

Fig. 15. Turbulence intensity distribution along the XoZ plane at instant time of 0.9 T. Left: LC1.1, right: LC3.1.

This phenomenon can be seen to start along the top surface of the foil, before continuing and extending to the trailing edge. We can see that both the recirculation regime (which is associated with a reversed pressure gradient) and the negative velocity regime become more profound as the flow moves from the foil root to the foil tip, with an increasing value of r/R. In addition, to illustrate the unsteady feature, Fig. 17 (b) plots the axial velocities at r/R = 20% for LC3.1 at different time instants between t = 0.9 T and t = 1.4 T, where the thrust increases gradually (see Fig. 11). As we can see from this figure, with the increase of incoming flow velocity, the flow separation near the trailing edge becomes weaker and weaker, leading to the increase of lift force and thus the overall thrust.

We can see that by comparing the pressure distribution shown in Fig. 18, that when the value of r/R is equal to 20%, LC3.1 is found to be significantly different than the other cases. This is especially noticeable at the regime x/Chord<0.5, suggesting that turbulence wind has a significant influence on the foil surface pressure distribution, which ultimately results in a change in the lift force and thrust/power. However, as the r/R value increases towards a value of 0.98 (where the blade slice ends up in its tip position), this discrepancy becomes less and less apparent. This finding then suggests that varying levels of turbulence will impact decays from the blade root to the blade tip. This conclusion is consistent with the turbulent boundary layer development around the slender shape of the blades and the turbine tower itself.

5.3. Shear wind layer thickness

We can see from the above results that there are a few distinct differences between the results gathered from uniform wind LC1.1, shear wind LC2.1 and LC2.2. If we consider the idea that a uniform wind can be treated as the shear layer height of zero, then we must conduct a further study to provide us with enough information to form a detailed explanation regarding to the impact of shear wind layer thickness to the FOWT aerodynamic.

Fig. 19 plots a zoom-in curve using the rotor thrust/power data shown previously in Fig. 11. There are three specific times selected for the purpose of plotting: $t_1 = 0.20$ T, $t_2 = 0.41$ T and $t_3 = 0.58$ T. These three times are selected as they correspond to the specific times at which a local minimum, maximum and moderate thrust/power appears, respectively.

From Fig. 19, we can see that regular local troughs and crests

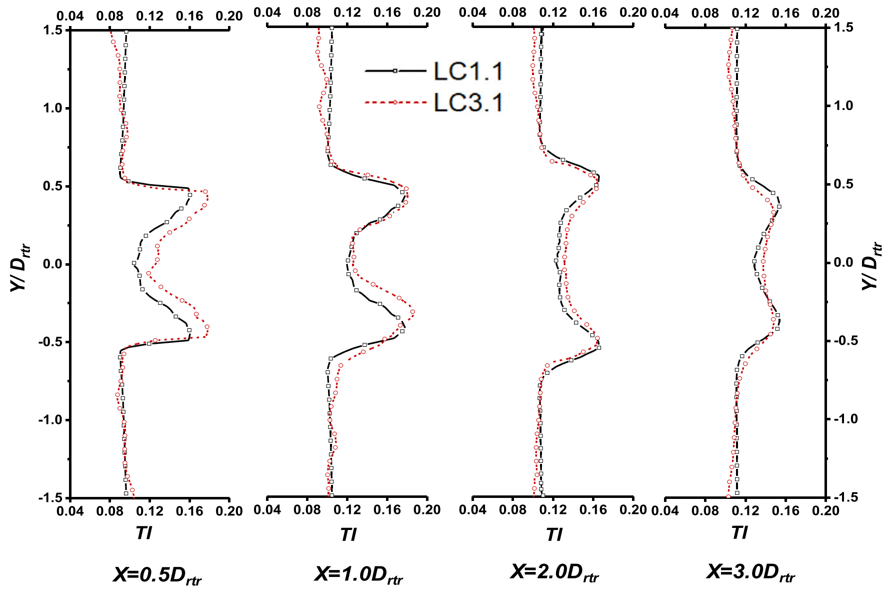

Fig. 16. Turbulence intensity at different axial positions at hub height (Z = 90 m) in the wake region at t = 0.9 T.

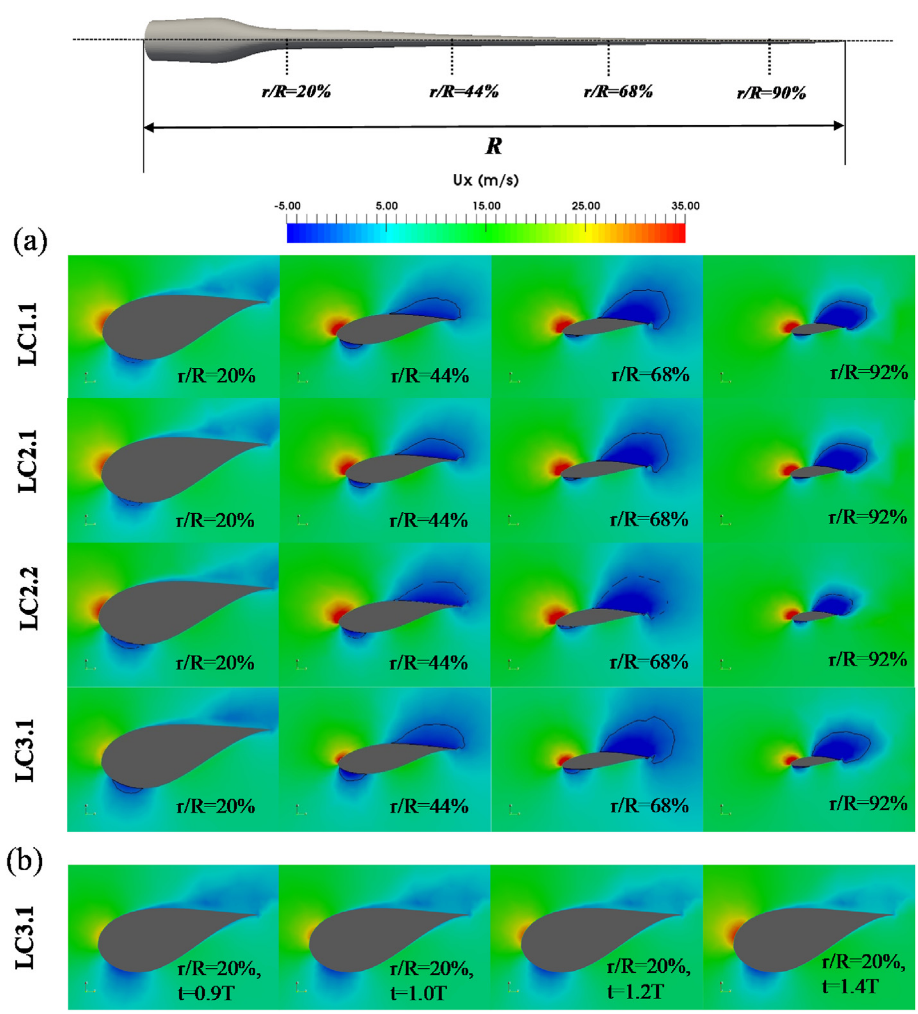

Fig. 17. Instantaneous flow field of (a) axial velocity along different blade sectional views at time t = 0.9 T (b) axial velocity along blade sectional views at r/R = 20% at different time instants for LC3.1.

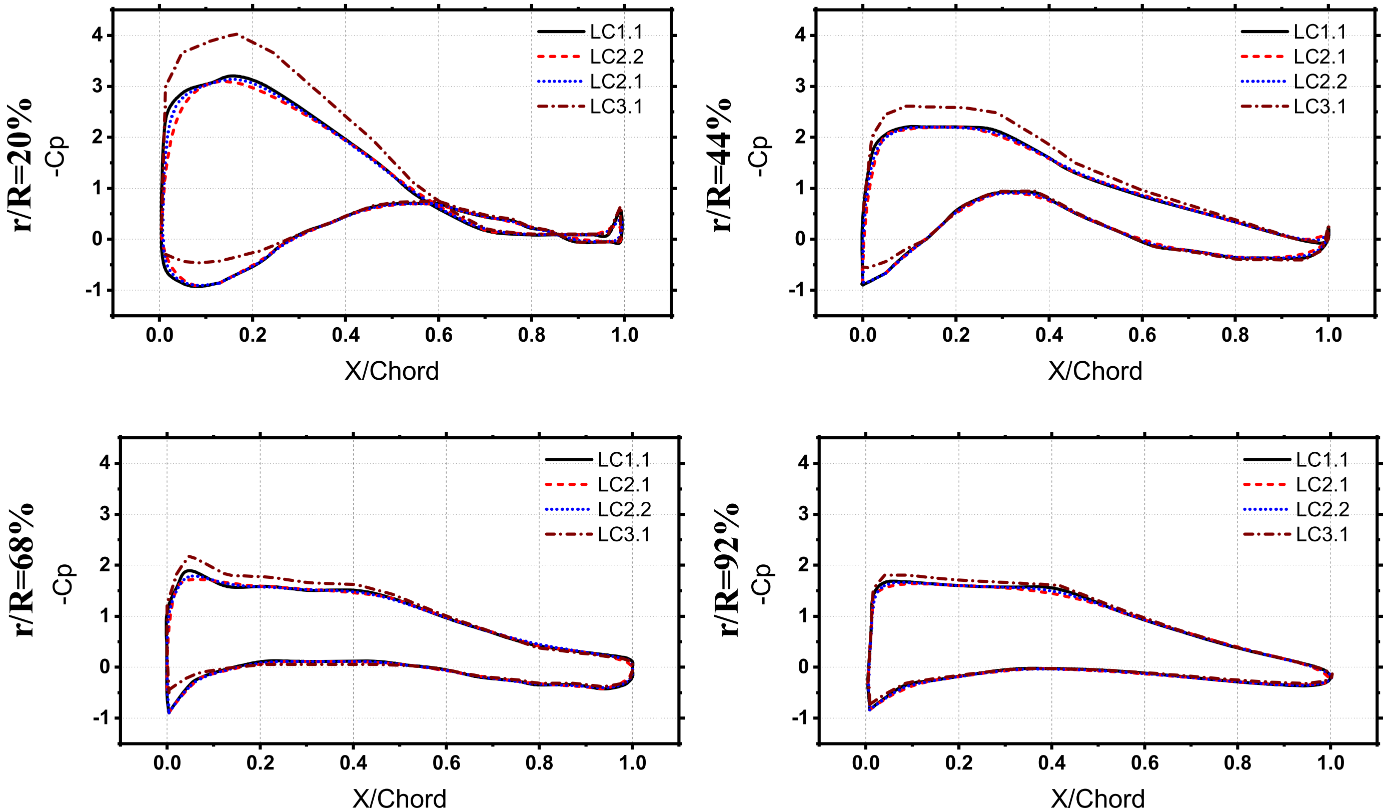

Fig. 18. Pressure distribution at different axial positions at instant time t = 0.9 T.

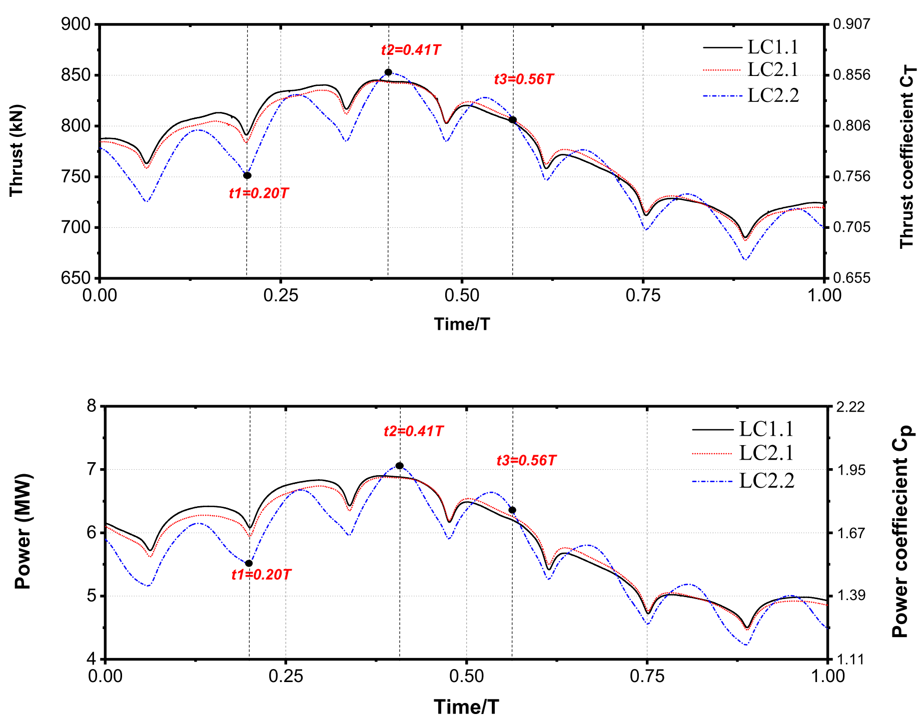

Fig. 19. Thrust and power outputs of FOWT under time independent wind fields.

develop in the time sequence thrust/power curve regardless of the height of the wind shear layer. The local minima at t = 0.20 T, 0.34 T, 0.48 T, etc. appear in the same time instances as when the blades pass in front of the tower. This phenomena can also be found in various previous studies [19,20,27], and it has been named as the tower shadow effect. When we compare between the three

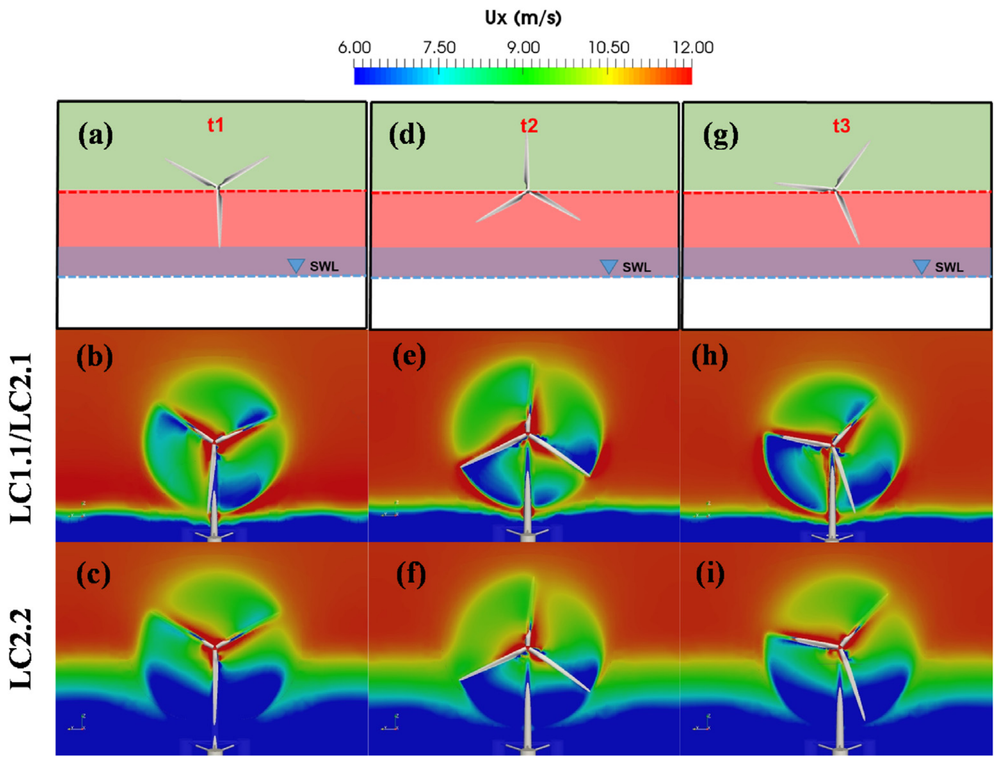

Fig. 20. The sketch of the turbine blade position and the instantaneous flow field at a vertical sectional plane (YoZ) at three time instances.

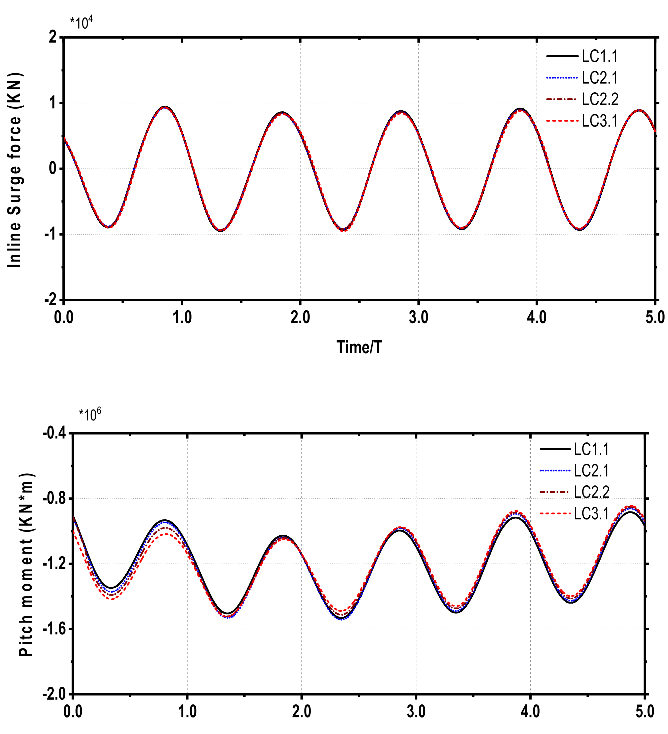

Fig. 21. Inline surge force and pitch moment of the FOWT under different wind fields.

different shear conditions, we can see that in all instances, LC2.2 always has a smaller thrust in comparison to the others. Since we know that the shear height of LC2.2 is 90 m, we can draw the conclusion that the shear thickness at this level has a significant impact on the aerodynamic characteristics of the wind turbine. This effect becomes most prominent at a time instance of $t_1 = 0.20$ T, where the thrust can be seen to decrease 6% from LC1.1 to LC2.2. The reasoning to explain this phenomenon can be found in the blade position and velocity contours displayed in Fig. 20. If we take the points $t_1 = 0.20$ T in Fig. 20 (a)–(c), we can see that in the low velocity zone (indicated by a large area coloured blue in Fig. 20 (c)) for LC2.2, this extends away from the platform towards the centre of the rotor. This low-speed regime is found to mainly occupy the area closest to wave-air free-surface for LC2.1 shown in Fig. 20 (b). As a result of this low speed regime, smaller wind turbine blades may generate lift force and thus resulting in a smaller torque and thrust.

One interesting thing to note is that as shown above, the shear layer impact is not always constant at any given time instance within a single wave cycle. We can see from Fig. 19, at specific time instances of $t = 0.34$ T, 0.48 T, 0.62 T, 0.76 T and 0.90 T, the shadow effect can also be spotted, similar to the occurrence at the point where $t_1 = 0.20$ T. In these instances however, it can be seen that the discrepancy among LC1.1, LC2.1 and LC2.2 is not as significant as $t_1 = 0.20$ T. Therefore, we can conclude that, at the mentioned time instances, the motion of the floater leads to the blade inclination to the incoming wind and also a reduced swept area of the turbine can be seen, resulting in the smaller thrust/power predictions.

Now, taking the point where $t_2 = 0.41$ T, the local peak thrust/power is achieved when the azimuth angle of the three blades are 0°, 120°, 240°, respectively. We can see that at this one moment, the disparity between LC1.1, LC2.1 and LC2.2 is extremely minimal. Compared with LC1.1 &2.1, the low velocity can be seen to occupy a slightly smaller area as displayed in Fig. 20 (e) & (f). Because of the decrease in the area which is occupies, it now has less of an impact on the thrust/power. This effect can be clearly seen at the point $t_3 = 0.58$ T in Fig. 20 (g)–(i), where the wind turbine is experiencing a moderate thrust/power, compared to the greater values which it

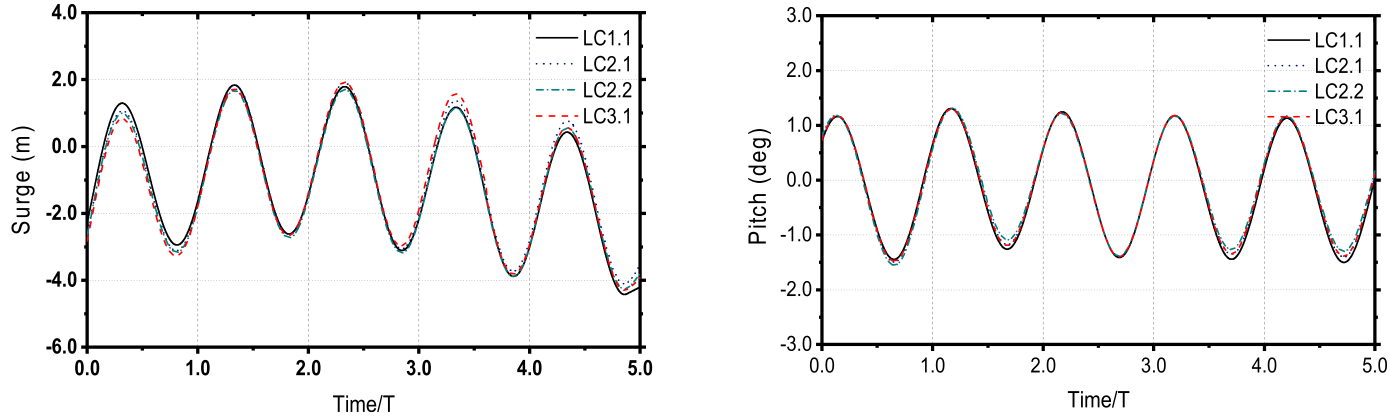

Fig. 22. Surge and pitch motion under different wind fields.

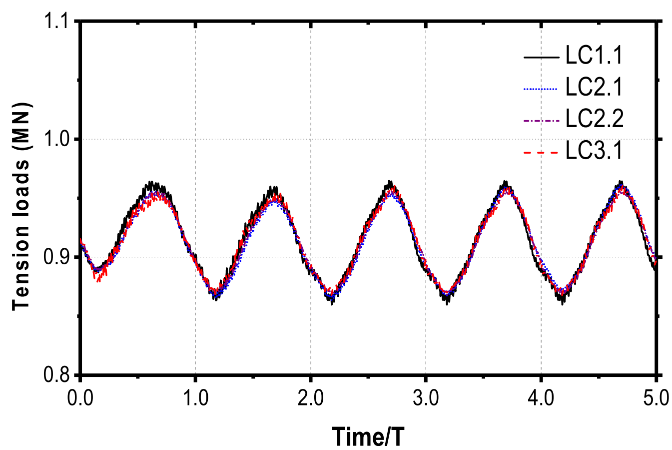

Fig. 23. Tension loads of one mooring line (connected with the larboard column) under different wind fields.

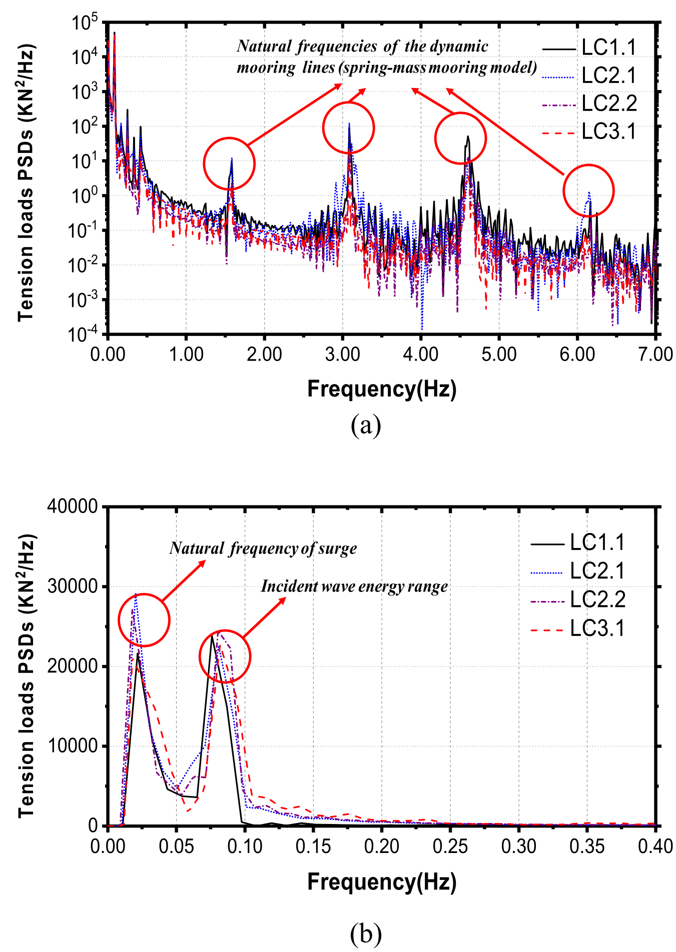

Fig. 24. PSDs of tension loads of the mooring line (connected with the larboard column) under different wind fields (a) log plots under the frequency range 0–7 Hz, (b) linear plots under the frequency range 0–0.4 Hz.

was previously experiencing.

5.4. Hydrodynamic response

Not taking into account the previously mentioned details regarding the aerodynamic of a wind turbine, the involvement of turbulent wind could also be influencing the FOWT hydrodynamic responses. Fig. 21 plots the inline surge force and the pitch moment relative to the tower root of the full FOWT under five sampled regular wave periods (132s–192s). From these results, we can conclude that the existence of different wind fields has little influence on the inline force and the pitch moment. Referring to Figs. 21 and 22, where the surge and pitch motion and mooring responses are plotted, we can see a similar trend occurs. Looking at the figures, we can deduct that the response amplitude/RAO is nearly identical regardless of whether the wind is uniform, shear or turbulent. Because of this, we can say that the turbulent wind has a negligible effect on the dynamic response of the FOWT substructure in the present study. This could be due to a relatively short-length numerical modelling conducted. It is anticipated that a much longer simulation may capture the low frequency loads induced by the turbulent wind at a very low resonance frequency closer to platform surge natural frequency. This time span for such simulation is around 30-50 periods of the floater natural motion periods, i.e. 900s–6000s, which is hard to be achieved using a high fidelity and computationally expensive CFD solver.

Lastly, in contrast to the fluctuation which could be seen previously in both the thrust and power curves in Fig. 11, here, we can see no such fluctuation on the curve of the floater. The lack of this fluctuation suggests that the excitation of the incident wave force and the tension of the mooring lines are the dominant factors alongside the dynamic motion responses of FOWT as well as the unsteady tension loading which can be seen in Fig. 23. In order to

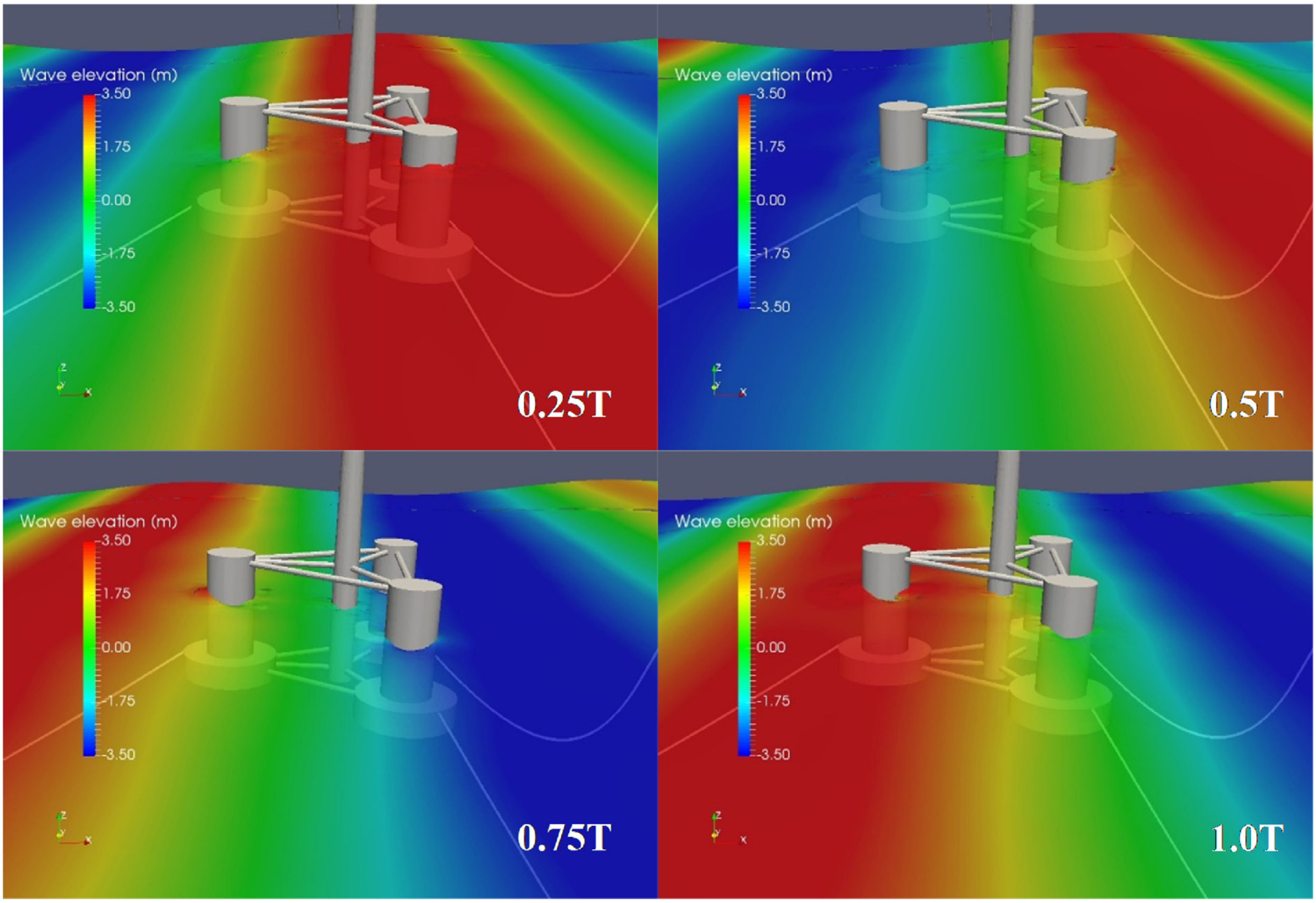

Fig. 25. Wave elevation contour plots around the FOWT within one wave period for LC1.1.

identify the frequency of the small oscillations observed in Fig. 23, we plot the PSDs of the mooring line tension loads in Fig. 24 (a) & (b). From Fig. 24 (a), it can be observed that the peaks inside the circle correspond to the natural frequency of mooring lines. The zoom-in plot in Fig. 24 (b) near the incident wave energy indicate the appearance of two peaks, one is at the platform surge natural frequency and another is at incident wave frequency.

Due to the fact that the hydrodynamic responses of the different wind fields are relatively similar to each other, the wave elevation CFD contour plots shown in Fig. 25 for LC2.1 have to be plotted within one sampled regular wave period (132s–144s). At the specific time instances of t = 0.25 T and 0.75 T, we can see that the floater experiences the maximum and minimum pitch motion, respectively. Looking at the plots, we can clearly see that the wave elevation varies as a direct consequence of a nonlinear wave-structure interaction, such as the wave diffraction or the wave radiation. These interactions are well caputured in the present simulation, evidenced by the detailed flow around upstream/side columns.

6. Conclusion and discussion

An investigation was carried out into an OC4 Semi-submersible NREL 5 MW FOWT and its performance under uniform, shear and turbulent wind conditions. This was done by using a blade-resolved CFD tool whilst factoring in the floating platform motion prediction. The investigation started with the generation of wind turbulence based on the Mann wind turbulence model, followed by a validation of the wind spectrum in comparison with the theoretical wind spectrum. Continuing from this, the study led onto the examination into the effects that wind turbulence has on the aerodynamic performance of the turbine i.e, how it influences the turbine and the dynamic responses of the floater.

The evidence gathered after comparison between turbulent wind and time-independent wind suggests that the existence of turbulence influences the airflow near the rotor blades, however, its impact on the time-mean flow around the turbine is minimal. The appearance of fluctuations on top of the time-mean thrust and power curve indicate that it is the presence of turbulence causes a larger standard deviation of power, as the value increases compared to when turbulence is absent. In addition, a large wind shear layer thickness results in a sudden drop of the local power in comparison to uniform wind. Despite this, it was found that neither wind turbulence nor wind shear had a significant impact on motion of the floater or the mooring tension loads. These findings are supported by further examinations conducted on the CFD predicted flow field around the wind turbine blades, wake and the wind-wave interactions near the wave-air free surface.

Aside from what is mentioned above, there are two points that should be also brought up. Firstly, the frequency of the turbulent wind in this study is quite a bit less than the floater's structural pitch/heave nature frequency of roughly 0.3 Hz. Thus, we can predict that the influence of turbulent wind on the floater dynamic responses is limited. Knowing this, we can anticipate that this conclusion will fluctuate if the turbulence frequency is adjusted closer to the FOWT eigenfrequencies, where the resonance of floater may occur. Secondly, the URANS method is used in this study. Due to the nature of Reynolds averaged of this tool, the predicted time-mean values are consistent with other low-fidelity methods. However, we are unable to capture the fine structure of the vortices under the Kolmogorov scale because of the large artificial dissipation embedded in URANS. Because of this, it may weaken our understanding of the vorticity interaction in the turbine wake.

CRediT authorship contribution statement

Yang Zhou: Writing – original draft, Conceptualization, Data processing, Methodology, Software. **Qing Xiao:** Writing – original draft, Supervision, Conceptualization. **Yuanchuan Liu:** Conceptualization, Investigation, Writing – review & editing, Validation, Software. **Atilla Incecik:** Supervision, Conceptualization. **Christophe Peyrard:** Writing – review & editing, Validation. **Decheng Wan:** Writing – review & editing, Supervision. **Guang Pan:** Writing – review & editing. **Sunwei Li:** Writing – review & editing.

Declaration of competing interest

The authors declare that they have no known competing financial interests or personal relationships that could have appeared to influence the work reported in this paper.

Acknowledgements

This work used the Cirrus UK National Tier-2 HPC Service at EPCC (http://www.cirrus.ac.uk) funded by the University of Edinburgh and EPSRC (EP/P020267/1) and ARCHIE-WeSt High Performance Computer (www.archie-west.ac.uk) based at the University of Strathclyde. Yang Zhou thanks China Scholarship Council (CSC) for financial support during his study in the UK.

References

[1] D. Roberts, These Huge New Wind Turbines Are a Marvel. They're Also the Future, Vox, 2019. May, 20.
[2] J. Larsson, S. Kawai, J. Bodart, I. Bermejo-Moreno, Large eddy simulation with modeled wall-stress: recent progress and future directions, Mechanical Engineering Reviews 3 (1) (2016), 15-418-415-418.
[3] Y. Fang, L. Duan, Z. Han, Y. Zhao, H. Yang, Numerical analysis of aerodynamic performance of a floating offshore wind turbine under pitch motion, Energy 192 (2020) 116621.
[4] J. Thé, H. Yu, A critical review on the simulations of wind turbine aerodynamics focusing on hybrid RANS-LES methods, Energy 138 (2017) 257–289.
[5] H. Lei, D. Zhou, Y. Bao, C. Chen, N. Ma, Z. Han, Numerical simulations of the unsteady aerodynamics of a floating vertical axis wind turbine in surge motion, Energy 127 (2017) 1–17.
[6] P. Veers, Modeling stochastic wind loads on vertical axis wind turbines, in: 25th Structures, Structural Dynamics and Materials Conference, 1984, p. 910.
[7] B.J. Jonkman, TurbSim User's Guide: Version 1.50, National Renewable Energy Lab.(NREL), Golden, CO (United States), 2009.
[8] J.M. Jonkman, M.L. Buhl Jr., FAST User's Guide, National Renewable Energy Laboratory, Golden, CO, 2005. Technical Report No. NREL/EL-500-38230.
[9] J. Mann, The spatial structure of neutral atmospheric surface-layer turbulence, J. Fluid Mech. 273 (1994) 141–168.
[10] L. Gilling, N.N. Sørensen, Imposing resolved turbulence in CFD simulations, Wind Energy 14 (5) (2011) 661–676.
[11] A. Chougule, J. Mann, A. Segalini, E. Dellwik, Spectral tensor parameters for wind turbine load modeling from forested and agricultural landscapes, Wind Energy 18 (3) (2015) 469–481.
[12] Y. Li, A. Castro, T. Sinokrot, W. Prescott, P. Carrica, Coupled multi-body dynamics and CFD for wind turbine simulation including explicit wind turbulence, Renew. Energy 76 (2015) 338–361.
[13] N. Troldborg, Actuator line modeling of wind turbine wakes, 2009.
[14] H. Olivares Espinosa, Turbulence modelling in wind turbine wakes, 2017.
[15] H.S. Chivaee, Large Eddy Simulation of Turbulent Flows in Wind Energy, DTU Wind Energy, 2014.
[16] C. Grinderslev, N.N. Sørensen, S.G. Horcas, N. Troldborg, F. Zahle, Wind turbines in atmospheric flow–FSI simulations with hybrid LES-IDDES turbulence modelling, Wind Energy Science (2020) 1–29.
[17] L. Li, Y. Liu, Z. Yuan, Y. Gao, Wind field effect on the power generation and aerodynamic performance of offshore floating wind turbines, Energy 157 (2018) 379–390.
[18] P. Doubrawa, M.J. Churchfield, M. Godvik, S. Sirnivas, Load response of a floating wind turbine to turbulent atmospheric flow, Appl. Energy 242 (2019) 1588–1599.
[19] D.S. Dolan, P.W. Lehn, Simulation model of wind turbine 3p torque oscillations due to wind shear and tower shadow, IEEE Trans. Energy Convers. 21 (3) (2006) 717–724.
[20] J. Cermak, J. Horn, Tower shadow effect, J. Geophys. Res. 73 (6) (1968) 1869–1876.
[21] B. Wen, S. Wei, K. Wei, W. Yang, Z. Peng, F. Chu, Power fluctuation and power loss of wind turbines due to wind shear and tower shadow, Front. Mech. Eng. 12 (3) (2017) 321–332.
[22] B. Gould, D. Burris, Effects of wind shear on wind turbine rotor loads and planetary bearing reliability, Wind Energy 19 (6) (2016) 1011–1021.
[23] Y. Fang, L. Duan, Z. Han, Y. Zhao, H.J.E. Yang, Numerical analysis of aerodynamic performance of a floating offshore wind turbine under pitch motion 192 (2020) 116621.
[24] H. Lei, D. Zhou, Y. Bao, C. Chen, N. Ma, Z.J.E. Han, Numerical simulations of the unsteady aerodynamics of a floating vertical axis wind turbine in surge motion 127 (2017) 1–17.
[25] Y. Liu, Q. Xiao, A. Incecik, C. Peyrard, D. Wan, Establishing a fully coupled CFD analysis tool for floating offshore wind turbines, Renew. Energy 112 (2017) 280–301.
[26] Y. Liu, PhD Thesis, in: A CFD Study of Fluid-Structure Interaction Problems for Floating Offshore Wind Turbines, University of Strathclyde, 2018.
[27] Y. Liu, Q. Xiao, A. Incecik, C. Peyrard, Aeroelastic analysis of a floating offshore wind turbine in platform-induced surge motion using a fully coupled CFD-MBD method, Wind Energy 22 (1) (2019) 1–20.
[28] Y. Zhou, Q. Xiao, Y. Liu, A. Incecik, C. Peyrard, S. Li, G. Pan, Numerical modelling of dynamic responses of a floating offshore wind turbine subject to focused waves, Energies 12 (18) (2019) 3482.
[29] OpenFOAM, The OpenFOAM foundation website, 2019.
[30] Menter, F., "Zonal two equation kw turbulence models for aerodynamic flows," Proc. 23rd Fluid Dynamics, Plasmadynamics, and Lasers Conference, p. 2906.
[31] C.W. Hirt, B.D. Nichols, Volume of fluid (VOF) method for the dynamics of free boundaries, J. Comput. Phys. 39 (1) (1981) 201–225.
[32] N.G. Jacobsen, D.R. Fuhrman, J. Fredse, A wave generation toolbox for the open-source libradry: OpenFOAM, Int. J. Numer. Methods Fluid. 70 (2012) 1073–1088.
[33] Fan, T., Qiao, D., and Ou, J., "Optimized design of equivalent truncated mooring system based on similarity of static and damping characteristics," Proc. The Twenty-Second International Offshore and Polar Engineering Conference, International Society of Offshore and Polar Engineers.
[34] J. Morison, J. Johnson, S. Schaaf, The force exerted by surface waves on piles, J. Petrol. Technol. 2 (5) (1950) 149–154.
[35] T. Von Karman, Progress in the statistical theory of turbulence, Proc. Natl. Acad. Sci. U.S.A. 34 (11) (1948) 530.
[36] S.B. Pope, Turbulent Flows, IOP Publishing, 2001.
[37] P.H. Madsen, D. Risø, Introduction to the IEC 61400-1 Standard, Risø National Laboratory, Technical University of Denmark, 2008.
[38] A.J. Coulling, A.J. Goupee, A.N. Robertson, J.M. Jonkman, H.J. Dagher, Validation of a FAST semi-submersible floating wind turbine numerical model with DeepCwind test data, J. Renew. Sustain. Energy 5 (2) (2013) 23116.
[39] J. Jonkman, S. Butterfield, W. Musial, G. Scott, Definition of a 5-MW Reference Wind Turbine for Offshore System Development, National Renewable Energy Lab.(NREL), Golden, CO (United States), 2009.
[40] N. Troldborg, J.N. Sørensen, R. Mikkelsen, N.N. Sørensen, A simple atmospheric boundary layer model applied to large eddy simulations of wind turbine wakes, Wind Energy 17 (4) (2014) 657–669.
[41] X. Tian, M.C. Ong, J. Yang, D. Myrhaug, Unsteady RANS simulations of flow around rectangular cylinders with different aspect ratios, Ocean Eng. 58 (2013) 208–216.
[42] B.J. Jonkman, M.L. Buhl Jr., TurbSim User's Guide, National Renewable Energy Lab.(NREL), Golden, CO (United States), 2006.
[43] S. Quallen, T. Xing, CFD simulation of a floating offshore wind turbine system using a variable-speed generator-torque controller, Renew. Energy 97 (2016) 230–242.
[44] T.T. Tran, D.-H. Kim, Fully coupled aero-hydrodynamic analysis of a semi-submersible FOWT using a dynamic fluid body interaction approach, Renew. Energy 92 (2016) 244–261.
[45] V. Kolář, Vortex identification: new requirements and limitations, Int. J. Heat Fluid Flow 28 (4) (2007) 638–652.